DISEASES AND DISORDERS

Astrocytes-derived LCN2 triggers EV-A71–induced muscle soreness via accumulating lactate

Qiao You[1]†, Jing Wu[1]†‡, Chaoyong Wang[2,3], Deyan Chen[1]¶, Shiji Deng[4], Yurong Cai[5], Nan Zhou[6], Ruining Lyu[1], Yajie Qian[7], Yi Xie[8]*, Miao He[9]*, Zhiwei Wu[1,9,10]*

Viral muscle soreness (VMS) is a common feature during acute viral infections, including those caused by enteroviruses, and it substantially diminishes patients' quality of life. At present, we aim to establish the "brain-muscle" axis to explore the underlying mechanisms of VMS. We initially observed that diminished pain threshold occurred in enterovirus A71 (EV-A71)–infected C57BL/6J and AG6 mice. Subsequently, RNA sequencing data showed that lipocalin 2 (LCN2) was up-regulated during multiple viral infections, including EV-A71, Japanese encephalitis virus, vesicular stomatitis virus, and West Nile virus, which all caused VMS. As expected, *Lcn2*-deficient C57BL/6 J (*Lcn2*$^{-/-}$) mice exhibited greater pain tolerance, as shown by stronger grip force and stable motor function after EV-A71 infection. Mechanistically, EV-A71–induced high-mobility group 1 (HMGB1) stimulated astrocyte-derived LCN2 secreted into the circulatory system, which enhanced glycolysis and induced lactate buildup in muscle through increasing pyruvate dehydrogenase kinase 1 (PDK1) expression and decreasing pyruvate dehydrogenase (PDH) activity. Together, HMGB1/LCN2/PDK1/lactate pathway in the brain-muscle axis promoted VMS development.

INTRODUCTION

Viral muscle soreness (VMS) is one of the most common symptoms at the onset of viral infectious diseases. VMS and associated fatigue occurred in various viral infections such as enterovirus (*1*), influenza virus (*2*), alphavirus (*3*), flavivirus (*4*), bunyavirus (*5*), and coronavirus (*6*). During viral infections, the presence of VMS can substantially diminish patients' quality of life. Remission of VMS is a key indicator for clinical assessment of the efficacy of antiviral agents. Therefore, considering the development benefits of antiviral agents, it is essential to investigate the underlying mechanisms of VMS, particularly the common mechanisms to different viruses.

VMS develops in the early stages of infection and varies with the severity of the infection (*7*). There is no direct evidence suggesting a causal relationship between the virus and muscle tissue infection in the occurrence of VMS, as VMS is also commonly observed in viral infectious diseases that do not primarily target muscle (*8*). Some opinions suggested that the virus-induced symptoms of muscle soreness and weakness may reflect altered central nervous system (CNS) function (*2*). However, nonmuscle predisposing viruses, including influenza, alphavirus, etc., are unlikely to infect nerves directly due to the tight blood-brain barrier (BBB) at the early stages of infection (*9*). A study on *Drosophila* with severe acute respiratory syndrome coronavirus 2 (SARS-CoV-2) protein injection in brain suggested that the "brain-muscle" signaling axis played an important role in muscle fatigue (*10*); therefore, there should be early response molecules as mediators of brain-muscle signaling transduction in VMS development.

Lipocalin-2 (LCN2), also known as neutrophil gelatinase-associated lipocalin, has been identified as an early mediator involved in various neurological diseases across different systems (*11*, *12*). Moreover, LCN2 is secreted into circulatory system and further causes tissue inflammation, which plays a crucial role in the onset and progression of pain (*13*–*16*). However, the roles of LCN2 in the brain-muscle axis-mediated VMS during viral infection remain largely unexplored, and the underlying mechanisms of this pathway are also intriguing.

LCN2 is also considered as a metabolic regulator and leads to cellular metabolic reprogramming in cancer or diabetes (*17*–*19*). Lactate accumulation is associated with pain sensation in muscle tissue. Mechanistically, muscle contraction requires energy generated from glucose catabolism, and disorders of glycolysis are associated with muscle cramps and weakness (*20*). The glycolysis results in the production of lactate and pyruvate, and pyruvate enters the tricarboxylic acid (TCA) cycle to produce adenosine 5′-triphosphate (ATP). However, glycolysis dysregulation-induced lactate accumulation lowered the pH in the tissues, activating acid-sensing ion channels and leading to a hypersensitivity response in the injury sensory system, which caused pain sensation (*18*, *21*, *22*). Lactate also promoted immune cell infiltration and production of proinflammatory cytokines (*23*), aggravating inflammation-mediated chronic muscle soreness (*24*). It is necessary to investigate the roles of dysregulation of glycolysis and lactate accumulation in VMS development, as well as the regulatory functions of LCN2 in lactate accumulation in muscle tissue.

Here, enterovirus A71 (EV-A71)—a causative agent of hand, foot, and mouth disease (HFMD) that often causes VMS—was used to

[1]Center for Public Health Research, Medical School of Nanjing University, Nanjing, China. [2]Northern Jiangsu People's Hospital, Yangzhou, Jiangsu, China. [3]Northern Jiangsu People's Hospital, Clinical Teaching Hospital of Medical School, Nanjing University, Yangzhou, China. [4]Department of Neurology, Drum Tower Hospital, Medical School and The State Key Laboratory of Pharmaceutical Biotechnology, Institute of Translational Medicine for Brain Critical Diseases, Nanjing University, Nanjing, China. [5]Ningxia Institute of Clinical Medicine, Central Laboratory, People's Hospital of Ningxia Hui Autonomous Region, Ningxia Medical University, Yinchuan, China. [6]Department of Dermatology, Nanjing Jinling Hospital, Affiliated Hospital of Medical School, Nanjing University, Nanjing, China. [7]Nanjing Stomatological Hospital, Medical School of Nanjing University, Nanjing, China. [8]Department of Neurology, Nanjing First Hospital, Nanjing Medical University, Nanjing, Jiangsu, China. [9]Yunnan Provincial Key Laboratory of Entomological Biopharmaceutical R&D, College of Pharmacy, Dali University, Dali, Yunnan, China. [10]State Key Laboratory of Analytical Chemistry for Life Science, Nanjing University, Nanjing, China.
*Corresponding author. Email: wzhw@nju.edu.cn (Z.W.); hemiao@dali.edu.cn (M.H.); yqxyk14@163.com (Y.X.)
†These authors contributed equally to this work.
‡Present address: Department of Preventive Medicine, School of Public Health, Fujian Medical University, Fuzhou, China.
¶Present address: Key Laboratory of Infection and Immunity of Anhui Higher Education Institutes, Bengbu Medical University, 2600 Donghai Avenue, Bengbu, Anhui, China.

establish VMS mouse model to investigate the mechanism of VMS development. We identified LCN2 as a mediator between brain and muscle, and *Lcn2* deficiency significantly alleviated the symptoms of muscle soreness during EV-A71 infection. Mechanistically, LCN2 was up-regulated and secreted from astrocytes at the early stages of virus infection, which was associated with virus-induced high-mobility group 1 (HMGB1) secretion (*25*). Subsequently, LCN2 induced lactate accumulation in muscle tissues via increasing pyruvate dehydrogenase kinase 1 (PDK1) expression and decreasing pyruvate dehydrogenase (PDH) activity. Overall, brain-muscle axis driven by HMGB1/LCN2/PDK1/lactate pathway may explain the development of VMS.

RESULTS

EV-A71 induced VMS both in AG6 and C57BL/6J mice

EV-A71, a highly neurotropic strain of the family Picornaviridae, is a positive-strand RNA virus, and patients with EV-A71–caused HFMD performed influenza-like muscle soreness (*26*). We have successfully established stable EV-A71–infected mouse model previously (*25*, *27*), and the EV-A71–infected AG6 mouse model allows us to investigate the pathogenic manifestations following viral infection (*28*). Initially, we performed the Von Frey test to determine the pain threshold, the grip strength test to measure the strength of limbs and the rotarod test to assess the motor coordination and balance of the EV-A71–infected [1.7×10^7 plaque-forming units (PFU) per mouse] AG6 mice at different days post-infection (dpi) (Fig. 1A). All the infected mice survived, and the body weight of mice was not affected following EV-A71 infection (Fig. 1, B and C). However, the pain threshold of mouse limbs decreased significantly from 4 dpi and persisted until 12 dpi (Fig. 1D). The grip force of the mice was also diminished from 4 to 12 dpi (Fig. 1E). In addition, EV-A71 infection caused a significant shortening of rotarod time at 4 and 12 dpi (Fig. 1F). Images of decreased motor activity of EV-A71–infected mice were recorded as shown in Fig. 1G. Next, we examined the pain threshold, grip strength, and rotarod running time in EV-A71–infected C57BL/6J mice (Fig. 1H), and the survival and the body weight of EV-A71–infected C57BL/6J mice were not affected (Fig. 1, I and J). The pain threshold of mouse limbs decreased from 2 dpi to the minimum at 5 dpi, then persisted until 7 dpi, and returned to normal levels at 12 dpi (Fig. 1K). However, the grip force and the running time of the C57BL/6J mice were not affected (Fig. 1, L to N). Overall, these results showed that EV-A71 infection induced VMS in AG6 and C57BL/6J mice, which was more pronounced in EV-A71–infected AG6 mice model.

Brain-derived LCN2 up-regulation was associated with VMS following viral infection

To investigate the mechanisms of EV-A71–induced muscle pain at the early stages of viral infection, we first determined the viral replication in different mice organs following EV-A71 infection. Viral RNA was significantly increased in the intestine at 4 dpi and in the brain at 12 dpi, whereas no viral RNA was detected in the muscle tissue of EV-A71–infected AG6 mice (Fig. 2A). Furthermore, in EV-A71–infected C57BL/6J mice model, EV-A71 RNA was primarily detected in the intestine at 1 and 3 dpi but not detected in the muscle or brain (Fig. 2B). These results suggested that the development of VMS was not directly related to EV-A71 replication in muscle, which implied that there must be a mediator that transmits signals from other organs, such as intestine or brain, to the muscle.

To explore the mediator between brain and muscle that contributes to VMS development at the early stages of EV-A71 infection, we re-analyzed the differentially expressed genes (DEGs) in several RNA viruses infections that relevant to VMS, including vesicular stomatitis virus (VSV) (*29*), Japanese encephalitis virus (JEV) (*30*), West Nile virus (WNV) (*31*), and EV-A71, from the Gene Expression Omnibus (GEO) database, and 31 common DEGs were identified in virus-infected mouse brain (Fig. 2, C and D). The Gene Ontology (GO) enrichment analysis showed that three DEGs (*Cd40*, *Serpine1*, and *Lcn2*) were involved in extracellular exosome/region/space (Fig. 2E), which might serve as mediators between brain and muscle. Previous reports showed that LCN2 was up-regulated after either influenza A virus (IAV) or SARS-CoV-2 infection and positively correlated with disease severity (*32*). Considering the secretion properties of protein, its corresponding roles in muscle and its association with viral infection, we selected LCN2 encoded by *Lcn2* for further investigation.

Subsequently, to determine the organ origin of LCN2 following EV-A71 infection, LCN2 mRNA levels were detected in the different tissues of EV-A71–infected AG6 mice. The LCN2 mRNA was notably up-regulated in the brain tissues while remained at basal level in the muscle, peripheral blood, intestine, or lungs, and the LCN2 secretion was increased in the brain tissues (fig. S1, A to I). In addition, LCN2 mRNA level was up-regulated by EV-A71 infection in human neural cell lines, such as T98G and U87MG cells (fig. S2, A to D). The above in vivo and in vitro evidence implied that EV-A71–induced LCN2 was primarily produced in brain. Next, LCN2 mRNA level was significantly increased in the brain tissue of EV-A71–infected mice, peaking at 2 dpi in AG6 mice and at 5 dpi in C57BL/6J mice, during EV-A71 infection (Fig. 2, F and I); the brain LCN2 protein levels increased from 4 dpi in AG6 mice and 1 dpi in C57BL/6J mice during EV-A71 infection (Fig. 2, G and J); the serum LCN2 levels lag behind brain tissue initially increased to peak at 4 dpi in AG6 mice and at 5 dpi in C57BL/6J mice during EV-A71 infection (Fig. 2, H and K). Together, these results illustrated that EV-A71–induced LCN2 initially and primarily expressed in brain and further secreted into circulatory system; however, the role of brain-derived LCN2 in EV-A71–related VMS development is largely unknown.

Therefore, we used C57BL/6J [wild-type (*WT*)] mice and *Lcn2* knockout mice ($Lcn2^{-/-}$) to investigate the role of LCN2 in EV-A71–induced VMS development (Fig. 3, A and G, and fig. S3). There was no significant difference in body weight between *WT* and $Lcn2^{-/-}$ mice without EV-A71 infection in 4 days (Fig. 3B). The $Lcn2^{-/-}$ mice showed higher mechanical threshold and greater grip force than *WT* mice; interestingly, recombinant mouse LCN2 (rmLCN2) addition significantly reduced the mechanical threshold in both $Lcn2^{-/-}$ mice and *WT* mice and diminished the grip strength of $Lcn2^{-/-}$ mice, but the grip strength of *WT* mice with rmLCN2 injection and the running capability of both $Lcn2^{-/-}$ and *WT* mice with rmLCN2 injection was not significantly affected (Fig. 3, C to F). Next, as shown in Fig. 3H, EV-A71 infection reduced the body weight of $Lcn2^{-/-}$ mice in 10 days; however, the $Lcn2^{-/-}$ mice showed statistically higher mechanical threshold and greater grip force than *WT* mice with EV-A71 infection (Fig. 3, I and J). The addition of rmLCN2 to $Lcn2^{-/-}$ mice reduced the mechanical threshold and diminished the grip strength (Fig. 3, I and J). $Lcn2^{-/-}$ mice showed longer running time than *WT* mice infected with EV-A71, and rmLCN2 injection significantly reduced the running time of the $Lcn2^{-/-}$ mice (Fig. 3, K and L). Overall,

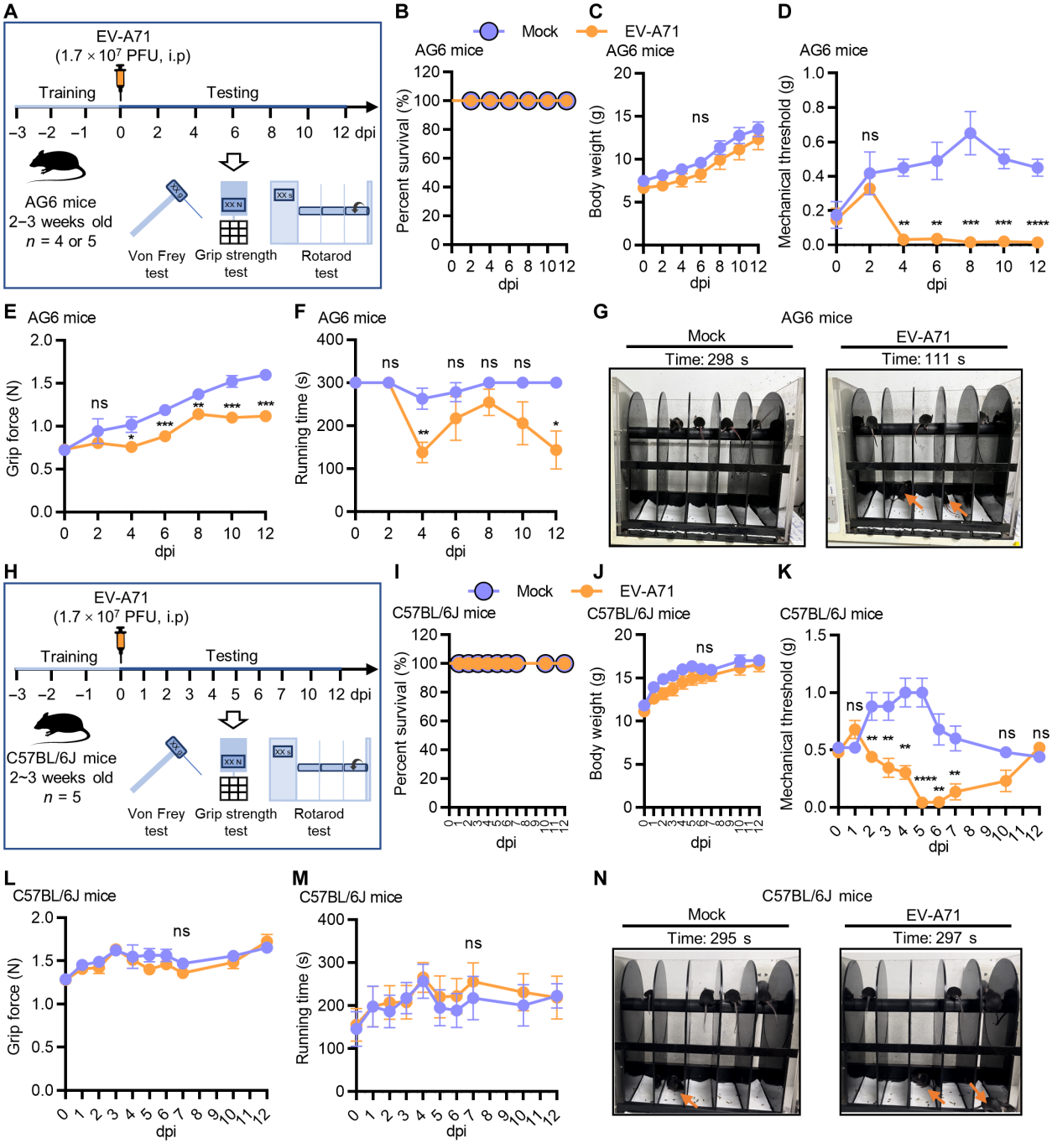

Fig. 1. EV-A71 infection induced muscle soreness in mice. (**A**) Experimental design for EV-A71–infected muscle soreness model in AG6 mice. Uninfected mice from the same litter were served as control (mock). $n = 4$ or 5. (**B** to **F**) Percent survival, body weight, mechanical threshold, grip force, and running time on rotarod of mock-infected mice and EV-A71–infected AG6 mice. (**G**) Records of running on a roller of mock-infected mice and EV-A71–infected AG6 mice at 12 dpi. Orange arrows indicated the dropped mice. (**H**) Experimental design for EV-A71–infected muscle soreness model in C57BL/6J mice. Uninfected mice from the same litter were served as control (mock). $n = 5$. (**I** to **M**) Percent survival, body weight, mechanical threshold, grip force, and running time on rotarod of mock-infected mice and EV-A71–infected C57BL/6J mice. (**N**) Records of running on a roller of mock-infected mice and EV-A71–infected C57BL/6J mice at 12 dpi. Error bars represent SEM. ns, not significant; $^{*}P < 0.05$; $^{**}P < 0.01$; $^{***}P < 0.001$; and $^{****}P < 0.0001$.

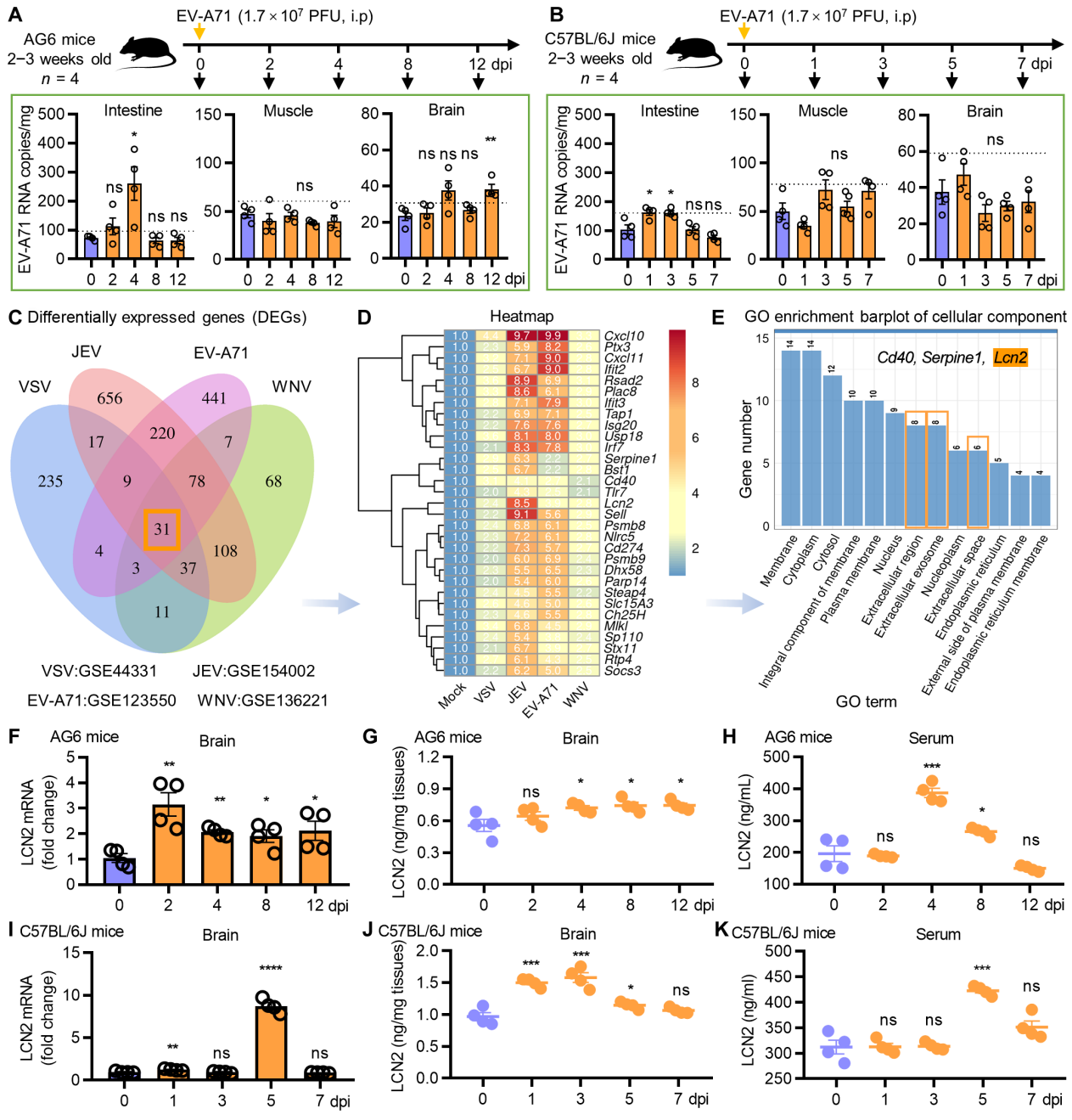

Fig. 2. LCN2 was secreted from brain following EV-A71 infection. (**A**) Experimental design for EV-A71–infected AG6 mice. EV-A71 RNA copies in harvested intestine, muscle, and brain tissues were quantified by absolute quantitative polymerase chain reaction (qPCR). $n = 4$. (**B**) Experimental design for EV-A71–infected C57BL/6J mice. EV-A71 RNA copies in harvested intestine, muscle, and brain tissues were quantified by absolute qPCR. $n = 4$. (**C**) Wayne's map showed the up-regulated DEGs numbers from VSV/JEV/EV-A71/WNV-related datasets in GEO. (**D**) Heatmap showed the 31 common up-regulated DEGs between mock-infected and VSV/JEV/EV-A71/WNV–infected mouse brain. The numbers in columns mean the logarithmic value of the average relative expression of genes of virus-infected group to mock-infected group. (**E**) GO enrichment barplot showed the cellular component of 31 common DEGs. The listed three genes were all included in the groups labeled by the orange box. (**F**) LCN2 mRNA levels in brain tissues from EV-A71–infected AG6 mice were quantified by qPCR, normalized to β actin. (**G** and **H**) LCN2 protein levels in the brain homogenization or serum of EV-A71–infected AG6 mice were determined by enzyme-linked immunosorbent assay (ELISA). (**I**) LCN2 mRNA levels in brain tissues from EV-A71–infected C57BL/6J mice were quantified by qPCR, normalized to β actin. (**J** and **K**) LCN2 protein levels in the brain homogenization or serum of EV-A71–infected C57BL/6J mice were determined by ELISA. Error bars represent SEM. ns, not significant, $^{*}P < 0.05$, $^{**}P < 0.01$, $^{***}P < 0.001$, and $^{****}P < 0.0001$.

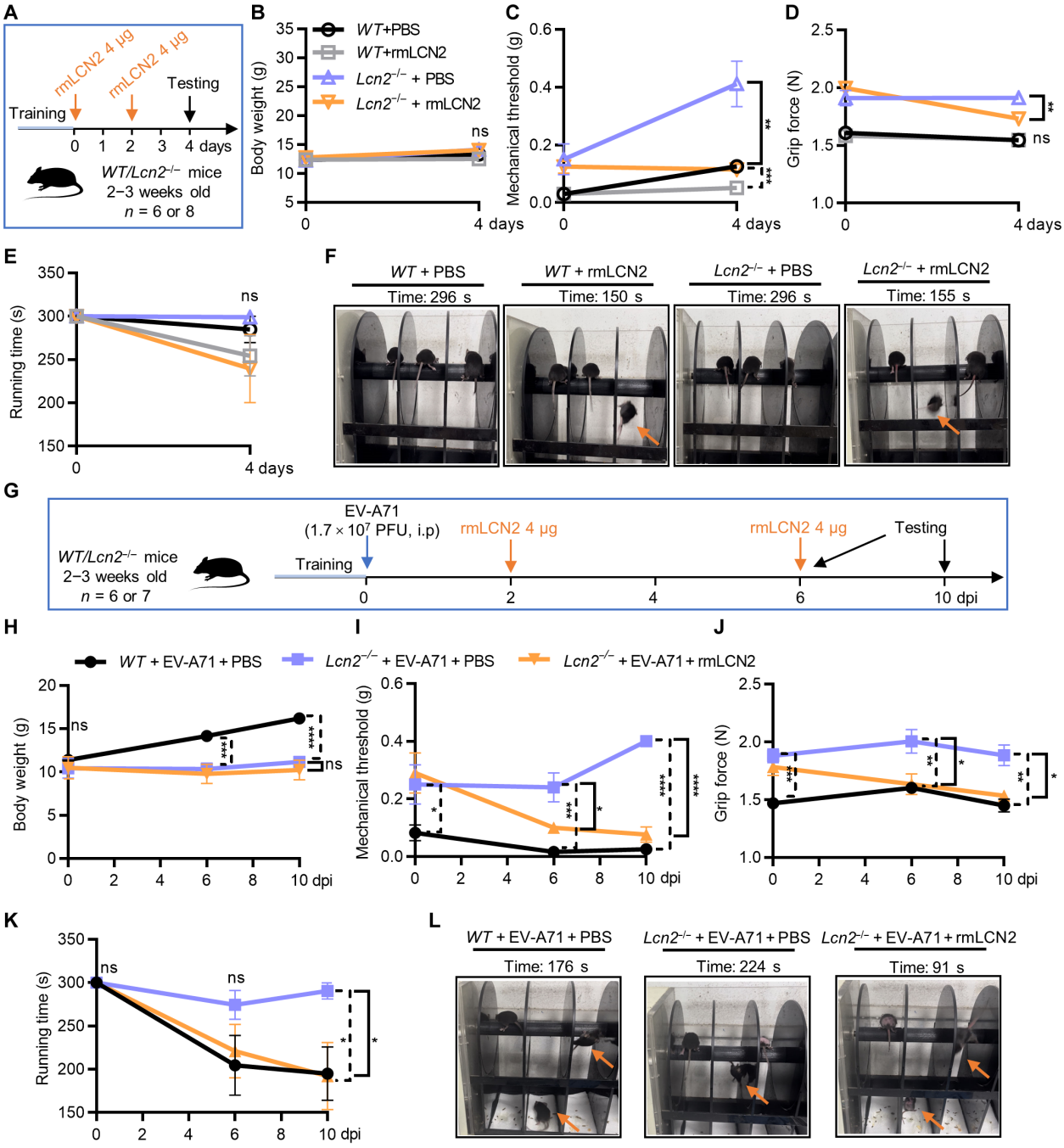

Fig. 3. LCN2 mediated muscle soreness following EV-A71 infection. (**A**) Experimental design for rmLCN2-stimulated mice model. Phosphate-buffered saline (PBS) injected mice were served as control. $n = 6$ or 8. (**B** to **F**) Body weight, mechanical threshold, grip force, running time on the roller, and the records of running on a roller of *WT* mice with PBS injection, *WT* mice with rmLCN2 injection, *Lcn2*$^{-/-}$ mice with PBS injection, and *Lcn2*$^{-/-}$ mice with rmLCN2 injection. (**G**) Experimental design for rmLCN2-stimulated and EV-A71–infected mice model. $n = 6$ or 7. (**H** to **L**) Body weight, mechanical threshold, grip force, running time on the roller, and the records of running on a roller of *WT* mice with EV-A71 infection and PBS injection, *Lcn2*$^{-/-}$ mice with EV-A71 infection and PBS injection, and *Lcn2*$^{-/-}$ mice with EV-A71 infection and rmLCN2 injection. Error bars represent SEM. ns, not significant; $^{*}P < 0.05$, $^{**}P < 0.01$, $^{***}P < 0.001$, and $^{****}P < 0.0001$.

LCN2 was primarily expressed in the brain and was subsequently secreted into the circulatory system as a mediator that induced VMS in the early stages of EV-A71 infection.

Brain-derived LCN2 was produced by astrocytes during EV-A71 infection

Astrocytes are the most abundant cell type in the brain and component of the BBB that maintain CNS homeostasis (*33*). EV-A71 and other viruses especially neurotropic viruses from the families Coronaviridae, Flaviviridae, and Picornaviridae tend to infect astrocytes to replicate and active astrocytes to secret inflammatory factors (*33*, *34*). To identify the source of LCN2 from which cell types it derived in the brain, we did immunofluorescence staining analysis of the whole brain (sagittal plane) sections of C57BL/6J mice and found that LCN2 was more frequent in choroid plexus, hypothalamus, and cerebral cortex (Fig. 4A), which is consistent with previous studies (*35*). Then, we detected LCN2 levels in individual astrocytes, microglia, and neuron in hypothalamic region of EV-A71–infected C57BL/6J mice (harvested at 5 dpi) and found that the mean fluorescence intensity of LCN2 in individual cells mostly increased in astrocytes, followed by microglia, but decreased in neurons following EV-A71 infection (Fig. 4B). In addition, LCN2 mRNA levels were down-regulated by EV-A71 infection in human neuroblastoma cell line SH-SY5Y (fig. S2, E and F). Collectively, these results suggested that astrocytes were the major neural cell type in which LCN2 expression was up-regulated following EV-A71 infection.

Virus-induced HMGB1 promoted LCN2 secretion from astrocytes

Given that EV-A71 failed to establish an infection in the brain tissue of C57BL/6J mice during the early stage of viral infection (Fig. 2B), yet LCN2 continued to be expressed and secreted (Fig. 2, I to K), we hypothesized that an intermediary molecule must be involved in this process. HMGB1 is a classical damage-associated molecular pattern, and we have reported that HMGB1 up-regulation was associated with BBB disruption and astrocytes activation in EV-A71–infected AG6 mice at the late time during EV-A71 infection (7 dpi) (*25*). The released HMGB1 acted as an inflammatory mediator in EV-A71 infection rather than affecting viral replication in vitro (*25*) and in vivo (fig. S4). We next investigated the role of HMGB1 on LCN2 secretion. Ahead of the temporal trend of LCN2 release in the serum, HMGB1 level was significantly increased during EV-A71 infection and peaked at 4 dpi in EV-A71–infected AG6 mouse serum (Fig. 5, A and B). In addition, this temporal trend of earlier release of HMGB1 than LCN2 in the serum was more pronounced in C57BL/6J mice, with HMGB1 levels remaining high from 1 to 5 dpi (Fig. 5, E and F). We then detected the HMGB1 protein levels in mouse brain and found that HMGB1 levels were increased at 2, 4, and 8 dpi in AG6 mice brain and elevated at 5 dpi in C57BL/6J mice brain, which were highly consistent with the increased LCN2 mRNA levels in the brain (Fig. 5, C and D and G and H). Furthermore, the intraperitoneal injection of recombinant mouse HMGB1 (rmHMGB1) protein increased the level of LCN2 in AG6 mice serum (Fig. 5, I and J). The immunofluorescent intensity of LCN2 (red) in brain tissues including cerebral cortex and hypothalamus was markedly increased together with the increased astrocytes activation (green) (Fig. 5, K and L). These results indicated that the peripheral HMGB1 stimulation was associated with LCN2 secretion from the astrocytes in vivo.

Next, we investigated the role of HMGB1 on LCN2 secretion from astrocytes in vitro. First, we collected the serum from EV-A71–infected AG6 mice at 0 or 4 dpi, then inactivated EV-A71 particles by ultraviolet (UV) irradiation, and added the serum to primary astrocytes isolated from AG6 mouse brain (validation was performed in fig. S5) in the presence of the nonspecific immunoglobulin M (IgM) (control IgM) or anti-HMGB1 neutralizing antibody (anti-HMGB1) (Fig. 6A). We found that the serum HMGB1 of infected mice increased the LCN2 secretion from primary astrocytes, and HMGB1-specific antibody neutralization not only reduced LCN2 mRNA levels but also decreased the LCN2 protein to the basal level (Fig. 6, B and C). Second, we used rmHMGB1 to stimulate primary astrocytes isolated from AG6 mouse brain (Fig. 6D) and found that rmHMGB1 (50 and 500 ng/ml) promoted LCN2 expression and secretion from primary astrocytes (Fig. 6, E and F). The similar promoting effect of HMGB1 on LCN2 expression and secretion was found in primary astrocytes derived from C57BL/6J mouse brain (Fig. 6, G to I and validation of primary astrocytes was shown in fig. S5). Third, we determined the effect of HMGB1 on LCN2 in U87MG cells by treating cells with the recombinant human HMGB1(rhHMGB1) (Fig. 6J) and found that the increased LCN2 mRNA and LCN2 secretion upon rhHMGB1 stimulation (Fig. 6, K and L). The similar results were found in T98G cells rather than SH-SY5Y (fig. S6). Last, as HT-29 cells were widely used as a cellular model to mimic EV-A71 intestinal infections (*25*), we next stimulated U87MG cells with cultural supernatant of EV-A71–infected HT-29 cells that contained HMGB1 (Fig. 6M) and found that the cultural supernatant up-regulated both the expression and secretion of LCN2 in U87MG cells (Fig. 6, N and O).

Given the enhanced LCN2 secretion induced by HMGB1, we next determined the role of HMGB1 on muscle soreness. The rmHMGB1 intraperitoneal injection significantly reduced the pain threshold of the *WT*/*Lcn2*$^{-/-}$ mice; on the contrast, *Lcn2* deficiency partly rescued the diminished pain threshold (Fig. 7, A and C). The body weight, the grip force, and the running time of *WT*/*Lcn2*$^{-/-}$ mice were not affected upon HMGB1 administration (Fig. 7, B and D and E). Furthermore, we detected the secretion of LCN2 upon HMGB1 stimulation in C57BL/6J mice and found that rmHMGB1 increased LCN2 levels in the brain and serum but not in the muscle, and *Lcn2* deficiency rescued the LCN2 levels (Fig. 7, F to H). Together, above evidence supported that nonbrain-derived HMGB1 induced brain-derived LCN2 expression and secretion at the early stage of EV-A71 infection, which then likely induced VMS via brain-muscle axis; therefore, we next focused on the mechanism by which the HMGB1/LCN2 pathway induced VMS via the brain-muscle axis.

EV-A71 infection induced muscular lactate accumulation to mediate VMS development

Glucose metabolism was important for muscle-producing energy for daily activities and played a key role in muscle soreness development. Given the association between muscle soreness development and EV-A71 infection, we investigated the impact of EV-A71 infection on glucose metabolism (Fig. 8A). Our results revealed that EV-A71 infection elevated levels of intercellular glucose, lactate, and pyruvate in vivo (Fig. 8, B to D) and decreased ATP production in vivo (fig. S7A). Lactate accumulation has been identified as an upstream event inducing muscle soreness (*36*); however, its role in the EV-A71–associated VMS development remains largely unknown. At present, exogenous lactate injection decreased the mechanical

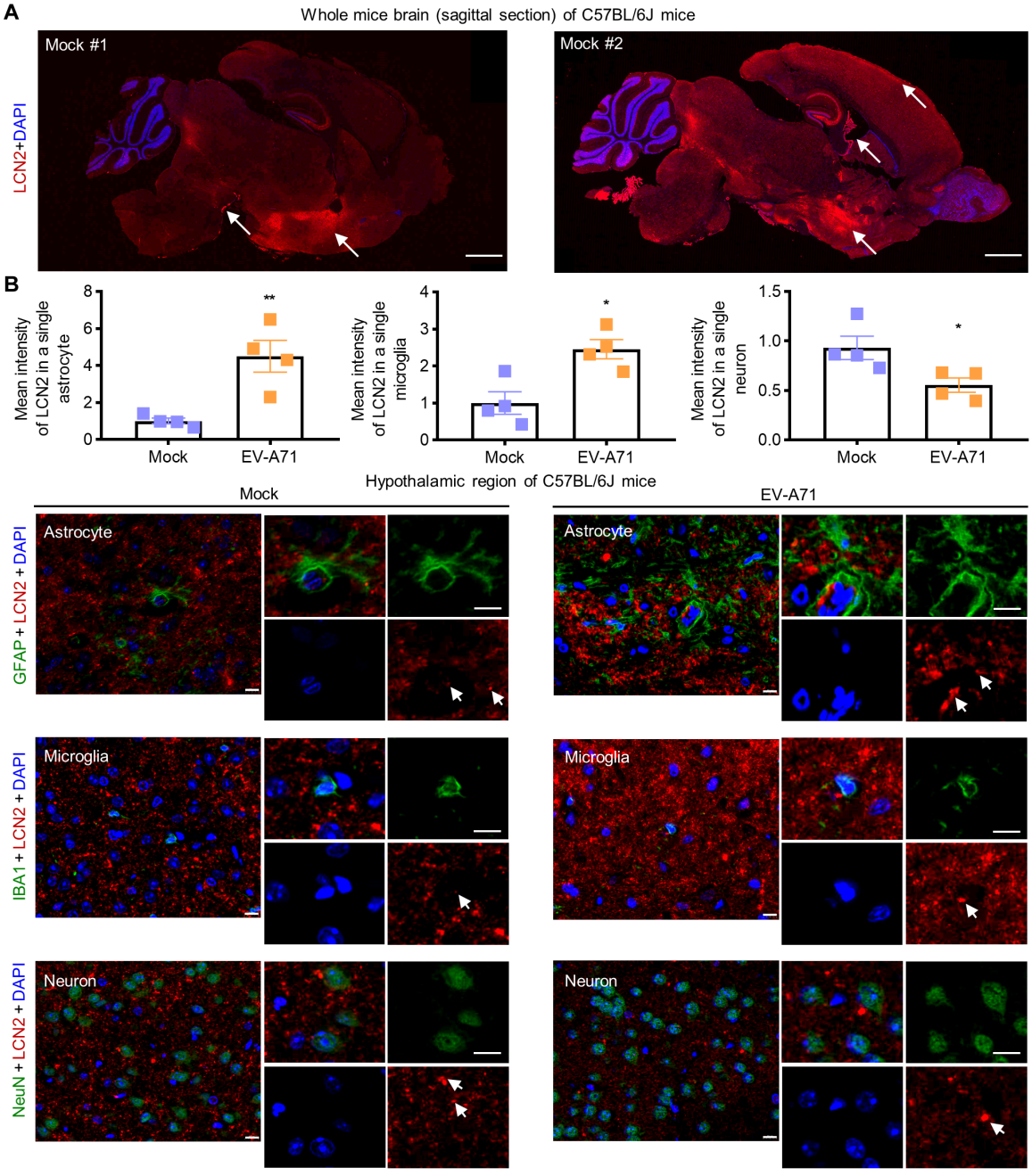

Fig. 4. LCN2 was secreted from astrocytes in brain. (**A**) Brain slices of mock-infected C57BL/67 mice were immunostained with antibodies against LCN2 (red). The nuclei were stained with 4′,6-diamidino-2-phenylindole (DAPI). Scale bars, 1000 μm. White arrows point to regions with abundant LCN2 expression. (**B**) Astrocytes, microglia, and neurons in the hypothalamic region of mock-infected and EV-A71–infected (harvested at 5 dpi) C57BL/6J mice ($n = 4$) were immunostained with antibodies against astrocyte-specific marker glial fibrillary acidic protein (GFAP) (green), microglia-specific marker ionized calcium binding adaptor molecule 1 (IBA1) (green), neuron-specific marker NeuN (green), and LCN2 (red). The nuclei were stained with DAPI. The scale bars in images and magnified images are 10 μm. The mean fluorescence intensity of LCN2 in individual astrocyte, microglia, and neuron (10 randomly selected cells) was quantified. Error bars represent SEM. *$P < 0.05$ and **$P < 0.01$.

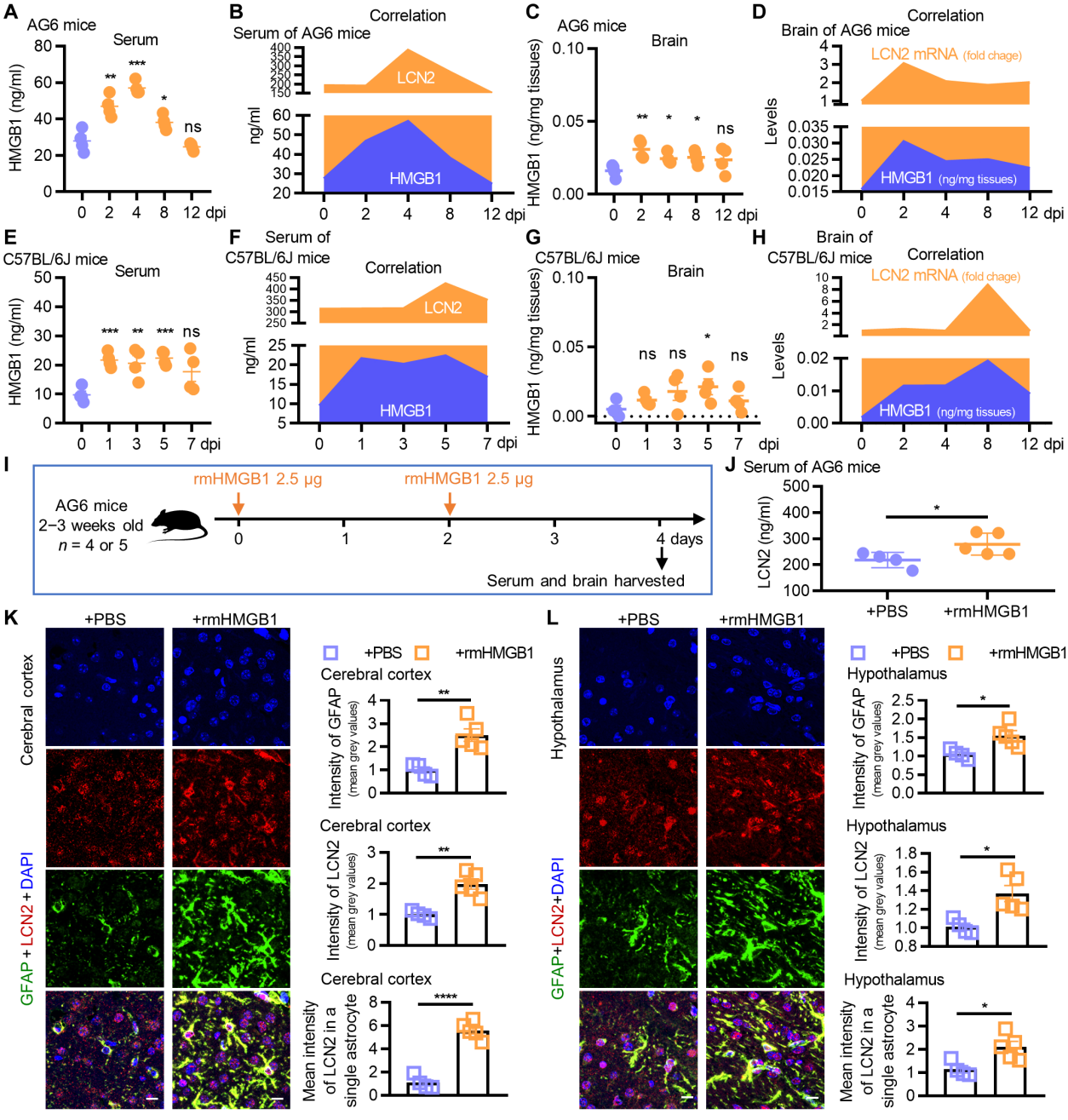

Fig. 5. HMGB1 was associated with the secretion of LCN2 from astrocytes. (**A**) HMGB1 protein levels in the serum of EV-A71-infected AG6 mice were determined by ELISA. (**B**) Correlation of HMGB1 and LCN2 levels in the serum of EV-A71-infected AG6 mice. (**C**) HMGB1 protein levels in the brain of EV-A71–infected AG6 mice were determined by ELISA. (**D**) Correlation of HMGB1 protein levels and LCN2 mRNA levels in the brain of EV-A71–infected AG6 mice. (**E**) HMGB1 protein levels in the serum of EV-A71–infected C57BL/6J mice were determined by ELISA. (**F**) Correlation of HMGB1 and LCN2 levels in the serum of EV-A71–infected C57BL/6J mice. (**G**) HMGB1 protein levels in the brain of EV-A71–infected C57BL/6J mice were determined by ELISA. (**H**) Correlation of HMGB1 protein levels and LCN2 mRNA levels in the brain of EV-A71–infected C57BL/6J mice. (**I**) Experimental design for rmHMGB1-stimulated AG6 mice model. PBS treatment was as control. $n = 4$ or 5. (**J**) LCN2 protein levels in the serum of rmHMGB1-stimulated mice on day 4 were determined by ELISA. (**K** and **L**) Cerebral cortex and hypothalamus of the brain tissues were immunostained with LCN2 antibodies (red) and astrocyte marker GFAP antibodies (green). The nuclei were stained with DAPI (blue). Scale bars, 10 μm. The intensity of GFAP and LCN2 and the mean intensity of LCN2 in individual astrocyte (10 randomly selected cells) were quantified by ImageJ software. Error bars represent SEM. ns, not significant; $^{*}P < 0.05$, $^{**}P < 0.01$, $^{***}P < 0.001$, and $^{****}P < 0.0001$.

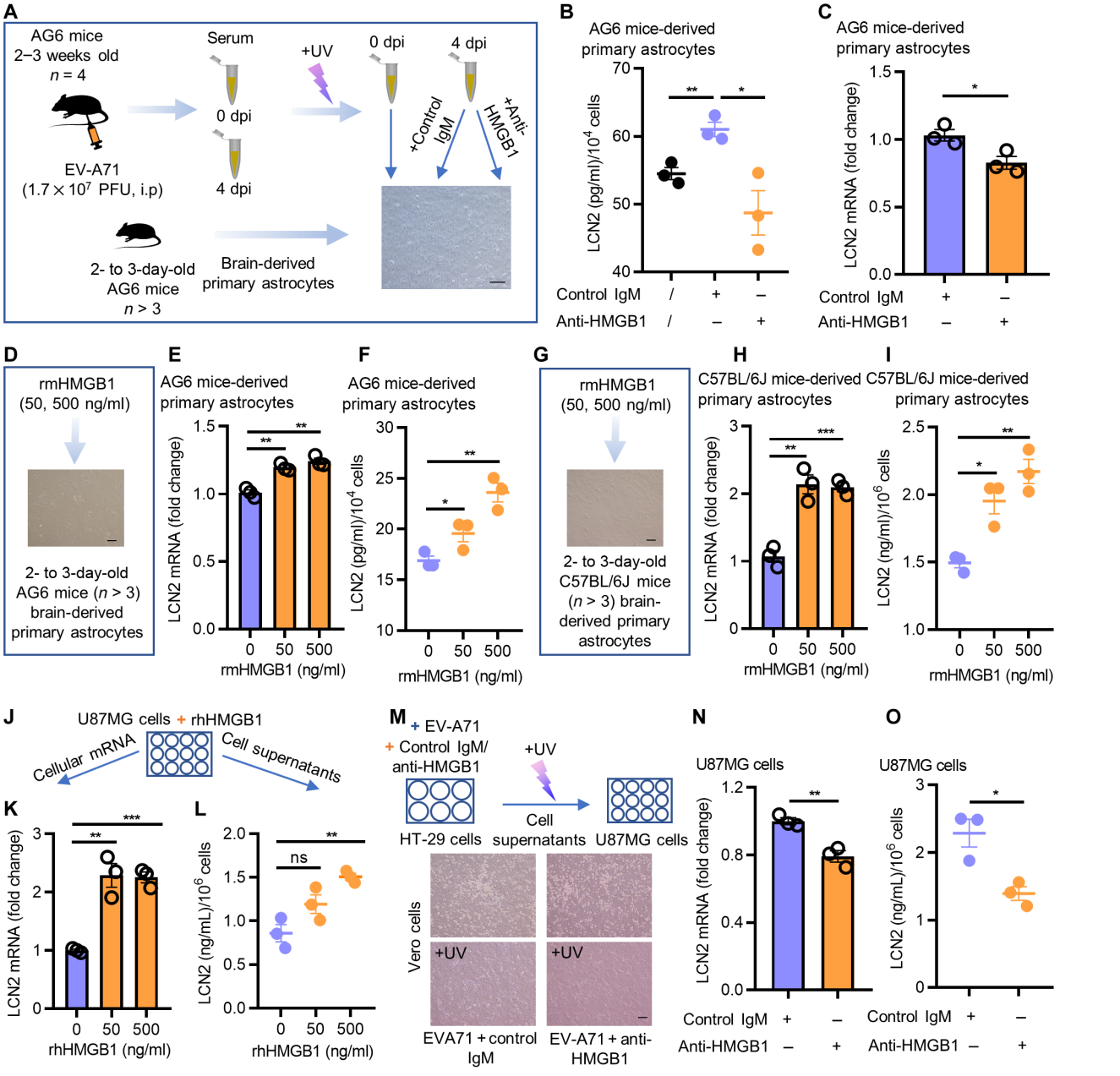

Fig. 6. HMGB1 promoted LCN2 secretion from astrocytes. (**A** to **C**) Experimental design for the neutralization of HMGB1 in EV-A71–infected mouse serum. Scale bar, 100 μm. The LCN2 levels in the cell supernatants of mouse-derived primary astrocytes were detected by ELISA. The LCN2 mRNA of primary astrocytes was quantified by qPCR, normalized by β actin. (**D** to **F**) rmHMGB1 protein was added to AG6 mice–derived primary astrocytes for 24 hours, then the cells were harvested for qPCR assay and normalized by β actin, the cell supernatants were collected for ELISA. Scale bar, 100 μm. (**G** to **I**) rmHMGB1 protein was added to C67BL/6J mice–derived primary astrocytes for 24 hours, then the cells were harvested for qPCR assay and normalized by β actin, and the cell supernatants were collected for ELISA. Scale bar, 100 μm. (**J** to **L**) U87MG cells were stimulated with rhHMGB1 protein for 24 hours, then the cellular mRNA was harvested for qPCR assay and normalized by β actin, and the cell supernatants were collected for ELISA. (**M** to **O**) Experimental design for the neutralization of HMGB1 in EV-A71–infected HT-29 cell supernatants. Scale bar, 100 μm. The LCN2 mRNA levels in U87MG cells were quantified by qPCR and normalized by β actin. The LCN2 protein levels in the cell supernatants of U87MG cells were detected by ELISA. Error bars represent SEM. ns, not significant; $^{*}P < 0.05$, $^{**}P < 0.01$, and $^{***}P < 0.001$.

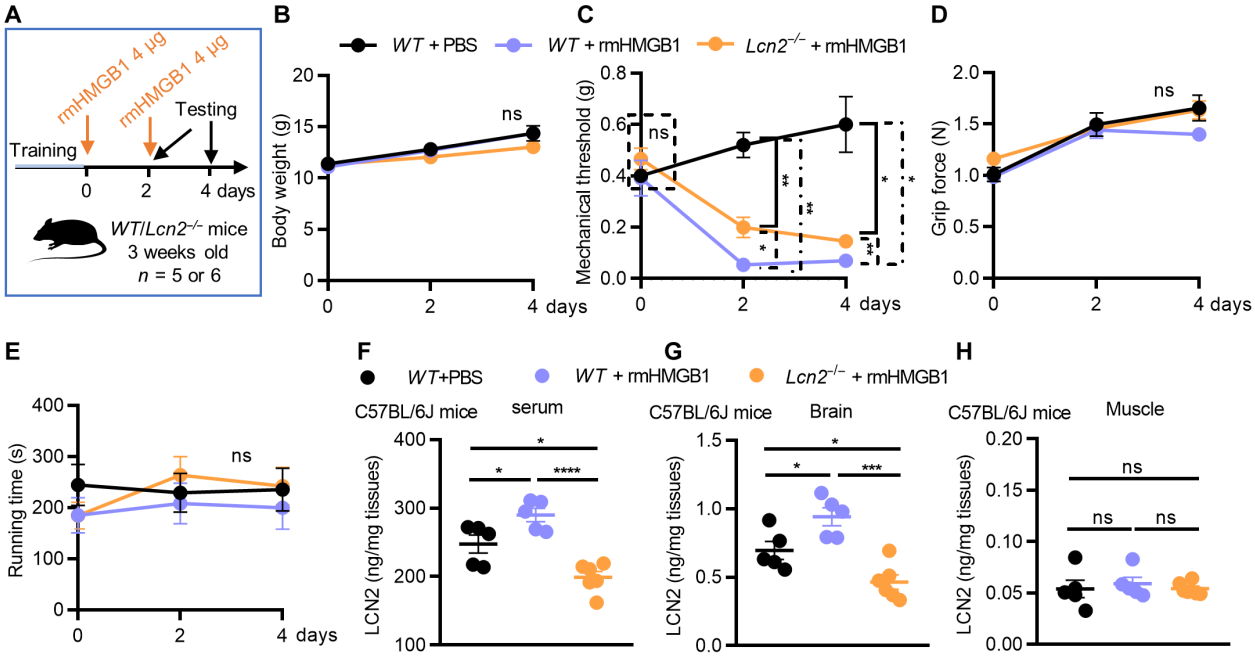

Fig. 7. HMGB1/LCN2 axis mediated muscle soreness. (**A**) Experimental design for rmHMGB1-stimulated mice model. PBS injection was served as control. $n = 5$ or 6. (**B** to **E**) Body weight, mechanical threshold, grip force, and running time on the roller of *WT* mice with PBS injection or rmHMGB1 injection and $Lcn2^{-/-}$ mice with rmHMGB1 injection. (**F** to **H**) The LCN2 protein levels in the serum, brain, and muscle (harvested on day 4) of *WT* mice with PBS injection or rmHMGB1 injection and $Lcn2^{-/-}$ mice with rmHMGB1 injection. Error bars represent SEM. ns, not significant; $^{*}P < 0.05$, $^{***}P < 0.001$, and $^{****}P < 0.0001$.

threshold of EV-A71–infected AG6 mice but did not affect grip force or running time (Fig. 8E). Overall, EV-A71 infection enhanced intracellular glycolysis, promoted lactate production, and contributed to VMS development.

HMGB1/LCN2 pathway induced muscular lactate accumulation to mediate VMS development

We next explored the effect of LCN2 on the glycolysis level. Recombinant human LCN2 (rhLCN2) increased the total ATP production rate but had no impact on the mitochondrial ATP production rate/glycol ATP production rate (fig. S7, B and C), while rhLCN2 significantly increased the extracellular acidification rate (ECAR) of rhabdomyosarcoma (RD) cells (Fig. 8F) and significantly increased the extracellular acidification by concentrations 200 and 400 ng/ml (Fig. 8G). Both rhLCN2 and plasmid encoding LCN2 increased the intracellular lactate concentration in vitro (Fig. 8, H and I). We then added UV-inactivated EV-A71 U87MG cell–conditioned media with or without anti-LCN2 neutralizing antibody (anti-LCN2) to RD cells and found that LCN2 derived from astrocytes increased lactate accumulation in RD cells (Fig. 8, J and K). Furthermore, the muscles of $Lcn2^{-/-}$ mice had lower glucose, lactate, and ATP levels compared to *WT* mice (Fig. 8, L and M, and fig. S7D), and the injection of exogenous LCN2 protein significantly increased the glucose, lactate, and ATP levels rather than pyruvate level (Fig. 8, L to N, and fig. S7D), suggesting that LCN2 increased glucose levels and lactate accumulation in muscle tissues.

Given the mediating role of the HMGB1/LCN2 pathway via the brain-muscle axis in VMS development (Figs. 5 to 7), we next tried to establish the HMGB1/LCN2/lactate axis. The injection of exogenous HMGB1 markedly increased the *WT* mouse muscular lactate levels, which were diminished by *Lcn2* deficiency (Fig. 8P), suggesting the HMGB1-stimulated lactate accumulation was dependent on LCN2. In addition, HMGB1 administration lower the ATP levels either in *WT* mice or $Lcn2^{-/-}$ mice (fig. S7E), but it did not affect the glucose and pyruvate level (Fig. 8, O and Q). Overall, these data demonstrated that HMGB1/LCN2 pathway promoted the lactate accumulation, which was involved in EV-A71–induced VMS development.

HMGB1/LCN2/PDK1/lactate axis mediated EV-A71–related VMS

The mechanism of HMGB1/LCN2 regulating the lactate accumulation is intriguing; therefore, we detected the expression of muscle-specific and glycolysis-associated genes upon rhHMGB1 or rhLCN2 stimulation. Both rhHMGB1 and rhLCN2 up-regulated hexokinase 2 (HK2), lactate dehydrogenase A (LDHA), and PDK1 mRNA expression in RD cells (Fig. 9, A and B), while UV-inactivated EV-A71 U87MG cell–conditioned medium with anti-LCN2 antibody treatment inhibited the expression of HK2 and PDK1 rather than LDHA (Fig. 9C). HK2 is the major hexokinases isoenzyme in skeletal muscle and catalyzes glucose to glucose-6-phosphate, the first step of glycolysis metabolism (*37*). PDK1 inactivates the PDH complex, thereby preventing the conversion of pyruvate to acetyl-coenzyme A, the critical step of lactate accumulation (*38*). The increased mRNA levels of HK2 and PDK1 were validated in muscles of rmHMGB1-injected *WT* mice muscle (Fig. 9D). However, the rmHMGB1 injection in $Lcn2^{-/-}$ mice only increased the HK2 mRNA levels but had no effect on PDK1 expression (Fig. 9E), which suggested that LCN2 was indispensable in the regulation of PDK1 by HMGB1. Moreover, *Lcn2*-lack mice muscle showed lower HK2 and PDK1 expression compared to *WT* mice (Fig. 9F), and rmLCN2 injection increased the HK2 and PDK1 expression in $Lcn2^{-/-}$ mice muscle (Fig. 9G).

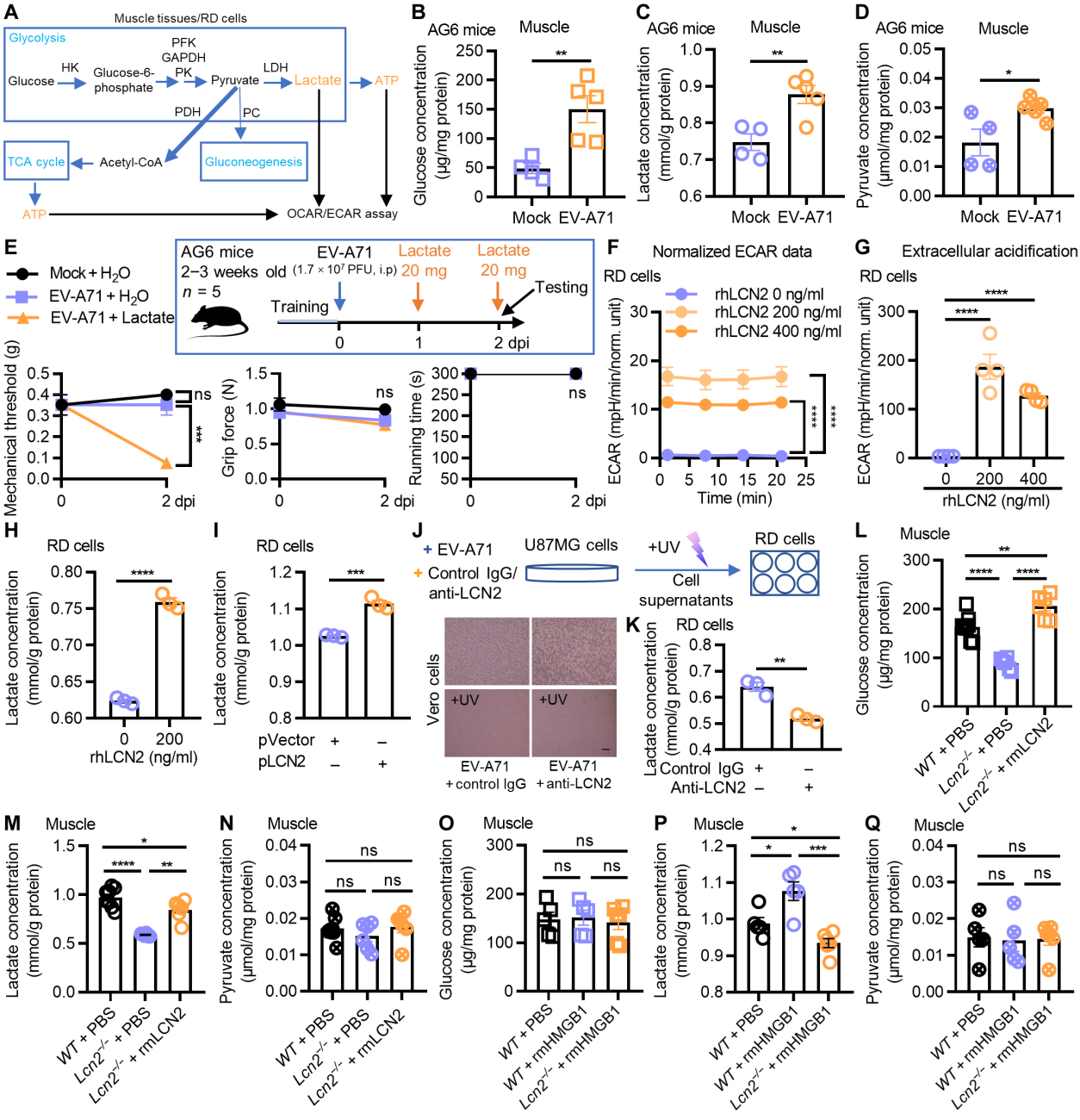

Fig. 8. HMGB1/LCN2 axis induced lactate accumulation to mediate EV-A71–induced muscle soreness. (**A**) Diagram of the glycolysis pathway and the production of lactate and ATP. (**B** to **D**) Glucose, lactate, and pyruvate concentration in muscle tissues of mock-infected and EV-A71–infected AG6 mice harvested at 4 dpi were detected by biochemical testing. $n = 4$ or 5. (**E**) Experimental design of lactate-stimulated and EV-A71–infected mice model. At 2 dpi, the mechanical threshold, grip force, and the running time on the roller of the mice were tested. $n = 5$. (**F** and **G**) RD cells in 96-well were stimulated with rhLCN2 for 24 hours, then the ECAR value was measured by ECAR/OCR assay. $n = 4$. (**H**) RD cells were stimulated with rhLCN2 for 24 hours, and then the lactate concentration in cells was detected by biochemical testing. (**I**) RD cells were empty vector–transfected or plasmid encoding LCN2 (pLCN2)-transfected for 30 hours, and then the lactate concentration in cells was detected by biochemical testing. (**J** and **K**) Experimental design of the neutralization of HMGB1 in EV-A71–infected U87MG supernatants. Scale bar, 100 μm. The lactate concentration in RD cells was determined by biochemical testing. (**L** to **N**) The tested muscle tissues were from *WT* mice, who were treated with PBS injection, and *Lcn2*$^{-/-}$ mice, who were treated with PBS injection or rmLCN2 protein injection in Fig. 3A. The glucose, lactate, and pyruvate concentration in muscle were determined by biochemical testing. $n = 6$ or 8. (**O** to **Q**) Tested muscle tissues were from *WT* mice, who were injected with PBS or rmHMGB1, and *Lcn2*$^{-/-}$ mice, who were injected with rmHMGB1 protein in Fig. 7A. The glucose, lactate, and pyruvate concentration in muscle were determined by biochemical testing. $n = 5$ or 6. Error bars represent SEM. ns, not significant; $^{*}P < 0.05$, $^{**}P < 0.01$, $^{***}P < 0.001$, and $^{****}P < 0.0001$.

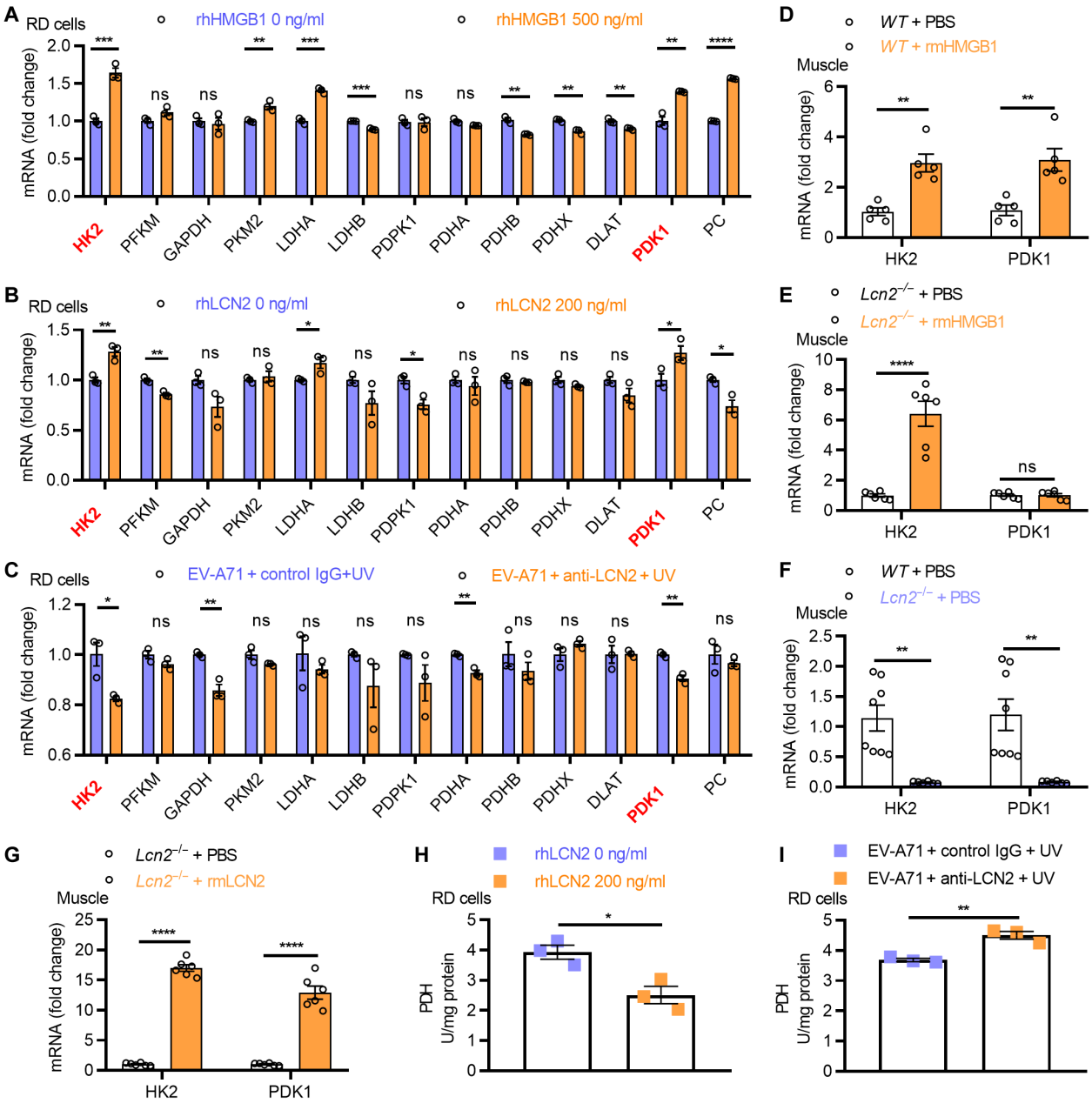

Fig. 9. HMGB1/LCN2 axis induced lactate accumulation via up-regulating PDK1 expression and reducing PDH activity. (**A**) RD cells were stimulated with rhHMGB1 for 24 hours, and then the mRNA levels of muscle-specific and glycolysis-associated genes including HK2, PFKM, GAPDH, PKM2, LDHA, LDHB, PDPK1, PDHA, PDHB, PDHX, DLAT, PDK1 and PC were quantified by qPCR and normalized by β actin. (**B**) RD cells were stimulated with rhLCN2 for 24 hours, and then the mRNA levels of muscle-specific and glycolysis-associated genes were quantified by qPCR and normalized by β actin. (**C**) Cell supernatants of EV-A71–infected and anti-LCN2/control IgG–incubated U87MG cells were treated with UV treatment and then were added to RD cells for 24 hours. The mRNA levels of the muscle-specific and glycolysis-associated genes were quantified by qPCR and normalized by β actin. (**D** to **G**) mRNA levels of HK2 and PDK1 in the muscle of *WT* mice with PBS or rmHMGB1 injection, the muscle of *Lcn2*$^{-/-}$ mice with PBS or rmHMGB1 injection, the muscle of *WT* mice with PBS injection and *Lcn2*$^{-/-}$ mice with PBS injection, and the muscle of *Lcn2*$^{-/-}$ mice with PBS injection or rmLCN2 protein injection were quantified by qPCR and normalized by β actin. (**H**) RD cells were stimulated with rhLCN2 for 24 hours, and then the enzyme activity of PDH in RD cells was detected by biochemical activity examination. (**I**) Cell supernatants of EV-A71–infected and anti-LCN2/control IgG–incubated U87MG cells were treated with UV treatment and then added to RD cells for 24 hours. The enzyme activity of PDH in RD cells was detected by biochemical activity examination. Error bars represent SEM. ns, not significant; **P* < 0.05, ***P* < 0.01, ****P* < 0.001, and *****P* < 0.0001.

In addition, rhLCN2 addition increased enzymatic activity of hexokinase (HK) (fig. S8A), and blocking released LCN2 from EV-A71–infected U87MG cells by anti-LCN2 antibody decreased the enzymatic activity of HK (fig. S8B). To investigate the role of LCN2 on glucose uptake, we used the fluorescent glucose analog 2-[*N*-(7-nitrobenz-2-oxa-1,3-diazol-4-yl) amino]-2-deoxyglucose (2-NBDG) and showed that LCN2 increased the glucose uptake (fig. S8C). Next, we detected the expression of glucose transporter type 1 (GLUT1) and glucose transporter type 4 (GLUT4), which are highly expressed in muscular cells (*39*). We found that *Lcn2* knockout decreased the muscular GLUT1 and GLUT4 mRNA expression, and LCN2 supplementation up-regulated muscular GLUT1 and GLUT4 in mouse (fig. S8, D and E). We further investigated the role of LCN2 on the enzymatic activity of PDH and found that rhLCN2 stimulation reduced, while blocking released LCN2 from EV-A71–infected U87MG cells by LCN2 neutralizing antibody increased the PDH activity (Fig. 9, H and I), indicating that LCN2 decreased pyruvate entering the TCA cycle. In addition, the LDH activity was actually decreased by rhLCN2 stimulation (fig. S9). Together, these results indicated that HMGB1/LCN2 axis promoted lactate accumulation by increasing PDK1 expression and decreasing PDH activity.

HMGB1 neutralization alleviated the VMS during EV-A71 infection

We conducted experiments to investigate the impact of HMGB1 neutralization using anti-HMGB1 antibody in EV-A71–infected C57BL/6J mice, and the results showed that HMGB1 neutralization alleviated the muscle pain of mice caused by EV-A71 infection at 5 to 7 dpi and reduced the serum LCN2 at 7 dpi. As a control, the antibody treatment did not affect the body weight of the EV-A71–infected mice (Fig. 10, A to D).

DISCUSSION

Muscle soreness is the most common clinical symptoms among multiple viral infectious diseases. Infections caused by enterovirus can affect the mobility and have a long-term sequela in severe cases (*40*), and the similar persistent fatigue was also induced by SARS-CoV-2 infection (*41*). However, although virus-induced mobility impairment and pathological manifestation of muscles are widely observed, there is little scientific explanation for the cause. Using a EV-A71–induced muscle soreness mouse model, our present study found that HMGB1/LCN2/PDK1 axis promoted lactate accumulation via brain-muscle axis, which contributed to VMS development (Fig. 10E). Because LCN2 mRNA levels were up-regulated in many RNA viral infections including VSV, JEV, and WNV, and LCN2 secretion was increased in IAV and SARS-CoV-2–infected human serum (*32*), these implicated that LCN2-mediated muscle soreness may be a common mechanism in RNA virus infections, which, although, needs experimental evidence.

Our current study revealed the existence of brain-muscle signaling axis resulting in virus-induced soreness, and this signaling axis also participated in SARS-CoV-2 protein-CNS injection-caused mice running fatigue (*10*). Although we observed the increased LCN2 in microglia, astrocytes in the brain were the major cell type secreting LCN2 upon EV-A71 infection. In addition, none of the other organs investigated secreted LCN2. Although EV-A71 is a neurotropic virus, viral RNA cannot be detected at the early stage of EV-A71 infection in our study, and some other viruses rarely infect the nervous system because of the tight BBB, while LCN2 expression was also increased in patients (*42*). It is suggested that the upstream events leading to the secretion of brain-derived LCN2 were not dependent on direct viral infection of the brain. Rather, there must be a mediator involved in the signaling transduction between virus-targeted tissues and brain. Our previous and current work found that the HMGB1 was increased in the serum upon EV-A71 infection. HMGB1 is an abundantly expressed alarm protein to response to multiple virus infections and other foreign pathogen invasion and typically releases from virus-susceptible organs to affect other organs (*43*). In our previous studies, the released HMGB1 acted as an inflammatory mediator to activate astrocytes in the brain during EV-A71 infection rather than affecting viral replication in vitro and viral titers in vivo (*25*). In this study, released HMGB1 promoted LCN2 secretion from astrocytes in vivo and in vitro.

Our previous study revealed the ability of HMGB1 to disrupt BBB integrity (*25*), and we found an increased LCN2 secretion in the serum of rmHMGB1-stimulated AG6 mice in the current study. Several published studies reported that LCN2 was increased in plasma after ischemic stroke and hemorrhage, which were all accompanied by BBB disruption (*44*). Although we do not know for sure if LCN2 can cross the BBB bidirectionally under normal conditions, damages to the BBB likely promote the release of LCN2 from the brain into the circulation.

The promoter region of LCN2 contains binding sites for nuclear factor κB (NF-κB), CCAAT/enhancer binding protein, and other transcription factors (*35*), and HMGB1 could induce the release of a variety of downstream signaling molecules through HMGB1–receptor for advanced glycation end products (RAGE)/toll-like receptor 4 (TLR4)–NF-κB signaling axis (*45*). However, how HMGB1 regulates LCN2 remains unclear and the underling mechanisms between HMGB/LCN2 axis require further investigation.

Lactate buildup generally occurs in the absence of oxygen; interestingly, we found that EV-A71 infection increased lactate accumulation, which also occurred in many other viruses (*46*). Although the relationship between lactate buildup and viral replication is not clear, our study suggests that the accumulated lactate lead to VMS. Mechanistically, HMGB1/LCN2 axis increased glucose uptake, the upstream ingredients of lactate production, by increasing the expression and enzymatic activity of HK and increasing the expression of glucose transporter GLUT1 and GLUT4, and promoted pyruvate convert to lactate by increasing PDK1 expression and declining PDH enzyme activity. PDH is a multimeric enzyme whose catalytic activity is regulated by PDK-mediated the phosphorylation status of the E1α subunit, and PDK up-regulation resulted in cellular lactate accumulation and excretion, contributing to the elevated circulating lactate in patients (*47*). Similar to our study, LCN2 enhanced PDK2 expression, which resulted in increased lactate in satellite glial cells (SGCs) and neurons of dorsal root ganglion (DRG) in diabetic mice (*18*). We also examined the mRNA levels of LDHA and lactate dehydrogenase B (LDHB), which are transcriptionally translated into LDH, and found that the expression of LDHA and LDHB was differentially regulated under rhLCN2 stimulation. The LDH activity was down-regulated upon rhLCN2 stimulation. Therefore, we do not think that LDH pathway plays a key role in the EV-A71–induced lactate accumulation. The up-regulation of PDK1 and the down-regulation of PDH activity are likely key regulatory pathways in the EV-A71–induced lactate accumulation in the current study.

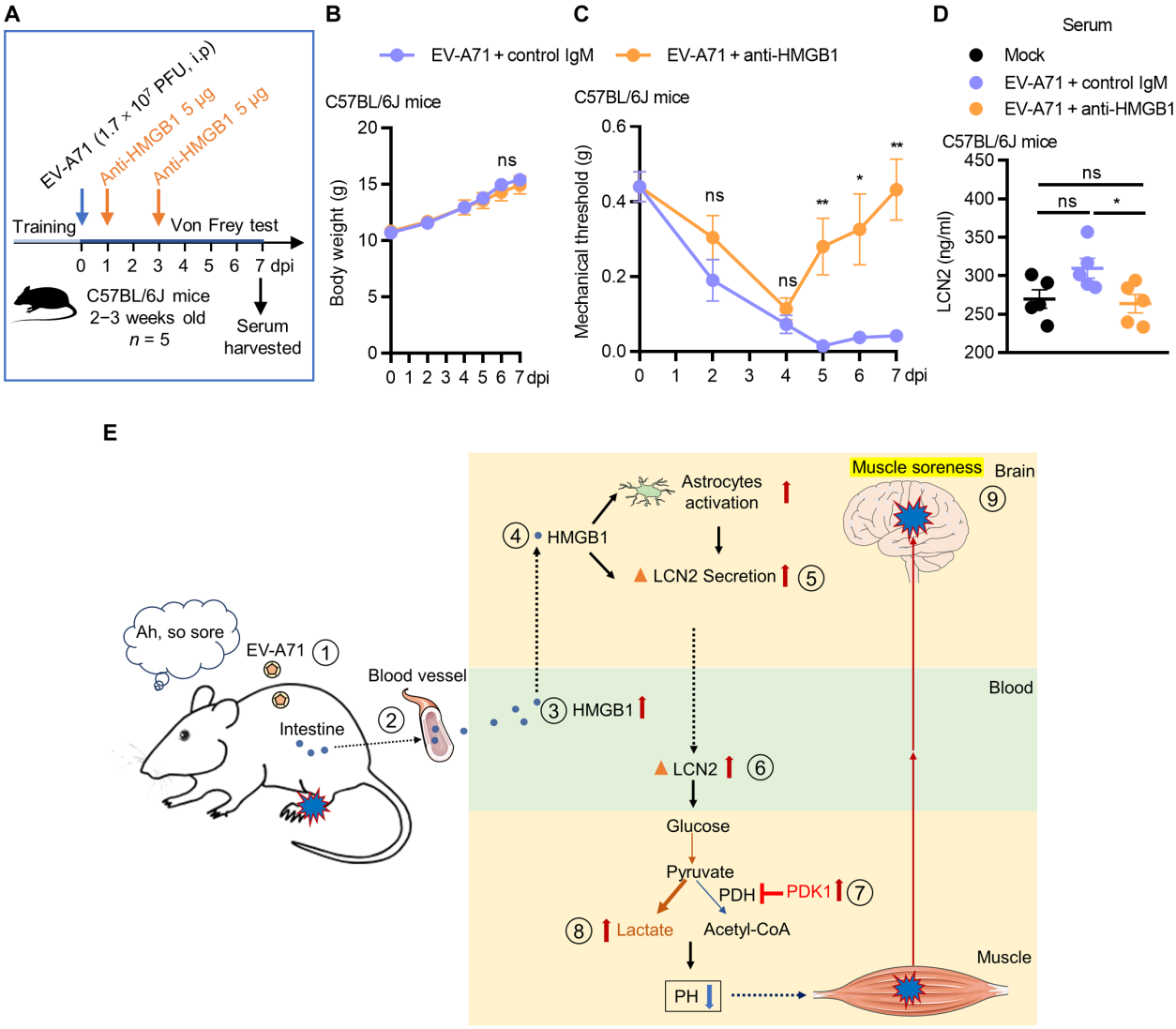

Fig. 10. Anti-HMGB1 addition attenuated VMS after EV-A71 infection. (**A**) Experimental design of anti-HMGB1–treated mice model. Control IgM injection was served as control. $n = 5$. (**B** and **C**) Body weight and mechanical threshold of C57BL/6J mice with control IgM injection or anti-HMGB1 injection. (**D**) LCN2 protein levels in harvested serum of C57BL/6J mice with control IgM injection or anti-HMGB1 injection at 7 dpi were determined by ELISA. Mock-infected mice serum was as control. Error bars represent SEM. ns, not significant; $^{*}P < 0.05$ and $^{**}P < 0.01$. (**E**) EV-A71 infection induced HMGB1 released to peripheral blood, and released HMGB1 promoted the secretion of LCN2 from activated astrocytes into the circulatory system. Mechanically, HMGB1/LCN2 axis mediated muscle soreness and promoted lactate accumulation in the muscle by up-regulating PDK1 expression and decreasing PDH activity.

Our study focused on exploring the effects of LCN2 on the metabolism of muscle tissue, with less attention paid to the effects of LCN2 on associated nerves. It was reported that astrocytes provided lactate to neuronal cells for energy supply (*48*), and the secreted LCN2 from astrocytes explored in this study may provide energy for neuronal activation by accumulating lactate in neurons; it was also reported that LCN2 secreted by activated astrocytes promoted neuron death (*49*); LCN2 released from high glucose-stimulated DRG SGCs damaged DRG neurons viability by increasing extracellular lactate concentration (*18*); thus, whether the effect of LCN2 secreted by astrocytes on muscle soreness is to promote or impair neuronal activation in the brain needs to be explored in the future. Furthermore, it was reported that the restoration of systemically low levels of survival motor neuron-1 protein specifically in astrocytes improved mouse survival, motor function, neuromuscular junction morphology, and vGLUT1^{+} synaptic bouton numbers, resulting in improved pathology of spinal muscular atrophy (*50*). Thus, the effect of secreted LCN2 from astrocytes on relevant neurons in the brain and the sensory nerve endings in muscle will be our future research direction.

In summary, our study revealed that astrocyte-derived LCN2 in the brain contributed to VMS, and peripheral HMGB1 was a mediator of LCN2 secretion. HMGB1/LCN2 axis promoted lactate accumulation via facilitating PDK1 expression and PDH activity, leading to muscle soreness.

MATERIALS AND METHODS

Mice

AG6 mice (type I/II interferon receptor deficient C57BL/6J mice) were donated by Q. Leng, at the Institute Pasteur of Shanghai.

C57BL/6J (*WT*) mice were purchased from the Yangzhou University Center for Comparative Medicine (Yangzhou, China). *Lcn2*$^{-/-}$ mice (B6.129P2-*Lcn2*^{tm1Aade}/AkiJ, the Jackson Laboratory, 024630) were obtained from the Jackson Laboratory. All the mice were housed in specific pathogen–free conditions. The light cycle of animal room is 12-hour light and 12-hour dark. All animal experiments were approved by Animal Care and Use Committee of Nanjing University. The research protocols in this study were conducted in accordance with the animal behavioral guidelines using protocols approved by the Institutional Animal Care Committee.

Animal behavioral tests

For each test, mice were acclimatized in the test chamber for 30 min. During habituation and throughout the test, light intensity was 150 to 200 lx, and the background white noise was 60 to 70 dB. All tests were performed at the same time of day.

Von Frey test

Pain threshold was determined using a set of 20 Von Frey filaments (Touch-Test Sensory Evaluators, North Coast Medical, lnc, CA) as described previously (*51*, *52*). Briefly, mice were placed under a transparent plastic box on a metal mesh floor, and a series of calibrated Von Frey hairs was applied to left and right hind paws to determine the stimulus intensity threshold stiffness required to elicit hind paw withdrawal responses. The 50% paw withdrawal threshold was measured by the Dixon up-down method (*53*). Mice will be trained for 3 days before familiarizition with the instruments.

Grip strength test

The strength of the fore and hind limbs of mice was measured by the grip strength meter (GS3, Bioseb, France). Mice were allowed to grasp the specially designed grid and pulled straightly in a line, and the maximal peak force was recorded as previously described (*54*). Mice will be trained for 3 days before familiarization with the instruments.

Rotarod test

The fixed speed mode of rotarod test typically assesses the motor coordination and the balance of mice on a rotating rod as previously described (*55*). Mice were placed on the rotarod apparatus (YSL-4C, Globalebio, Beijing, China) and allowed to freely move at 30 or 40 rpm for 5 min. Latency to fall was measured when the mice fell off the pole or rode in a continuous circle on the cylinder without regaining control. Mice will be trained for 3 days before formal testing to achieve a uniform baseline, which the mice could run for 5 min on the running wheel rotating at 30 rpm without falling off. Each testing day consisted of three attempts with a 30-min rest in between each trial.

Animal treatment protocol

For EV-A71–infected muscle soreness model in AG6 mice, 2- to 3-week-old AG6 male mice were trained with Von Frey test, grip strength test, and rotarod test for 3 days before EV-A71 infection (−3, −2, and −1 dpi) to reach the uniform baseline. Then mice were intraperitoneally injected with EV-A71 at 1.7×10^7 PFU in each mouse, and the behavioral tests were displayed at 0, 2, 4, 6, 8, 10, and 12 dpi.

For EV-A71–infected muscle soreness model in C57BL/6J mice, 2- to 3-week-old C57BL/6J male mice were trained with Von Frey test, grip strength test, and rotarod test for 3 days (−3, −2, and −1 dpi) to reach the uniform baseline. Then, mice were intraperitoneally injected with EV-A71 at 1.7×10^7 PFU in each mouse, and the behavioral tests were displayed at 0, 1, 2, 3, 4, 5, 6, 7, 10, and 12 dpi.

For EV-A71–infected AG6 mice, 2- to 3-week-old AG6 male mice were intraperitoneally injected with EV-A71 at 1.7×10^7 PFU in each mouse, and the serum and organ tissues were harvested at 0, 2, 4, 8, and 12 dpi.

For EV-A71–infected C57BL/6J mice, 2- to 3-week-old C57BL/6J male mice were intraperitoneally injected with EV-A71 at 1.7×10^7 PFU in each mouse, and the serum and organ tissues were harvested at 0, 1, 3, 5, and 7 dpi.

For LCN2 protein-stimulated mice model, 2- to 3-week-old *WT* male mice or *Lcn2*$^{-/-}$ male mice were trained with Von Frey test, grip strength test, and rotarod test for 3 days (−3, −2, and −1 days) to reach the uniform baseline. Then, mice were intraperitoneally injected with rmLCN2 at 4 μg per mouse on day 0 and day 2. On day 4, the mice were supplied to behavioral tests.

For LCN2 protein-stimulated and EV-A71–infected mice model, 2- to 3-week-old *WT* male mice or *Lcn2*$^{-/-}$ male mice were trained with behavioral tests for 3 days (−3, −2, and −1 dpi) to reach the same baseline. Next, the mice were intraperitoneally injected with EV-A71 at 1.7×10^7 PFU per mouse on day 0 and stimulated with rmLCN2 at 4 μg per mouse on day 2 and day 6. Then, on day 6 and day 10, the mice were supplied to behavioral tests.

For HMGB1 protein-stimulated AG6 mice model, 2- to 3-week-old AG6 male mice were intraperitoneally injected with rmHMGB1 at 2.5 μg per mouse on day 0 and day 2. Then, on day 4, the serum and brain tissues were harvested.

For lactate-stimulated and EV-A71–infected mice model, 2- to 3-week-old AG6 mice were trained with behavioral tests for 3 days (−3, −2, and −1 dpi) to reach the same baseline. Next, the mice were intraperitoneally injected with EV-A71 at 1.7×10^7 PFU per mouse on day 0 and stimulated with sodium L-lactate (L7022, Sigma-Aldrich, Darmstadt, Germany) at 20 mg per mouse on day 1 and day 2. Then, on day 2, the mice were supplied to behavioral tests.

For HMGB1 protein-stimulated mice model, 2- to 3-week-old *WT* male mice or *Lcn2*$^{-/-}$ male mice were trained with Von Frey test, grip strength test, and rotarod test for 3 days (−3, −2, and −1 days) to reach the uniform baseline. Then, mice were intraperitoneally injected with rmHMGB1 at 4 μg per mouse on day 0 and day 2. On day 4, the mice were supplied to behavioral tests.

For anti-HMGB1–treated mice model, 2- to 3-week-old *WT* male mice were pretrained with Von Frey test for 3 days. Next, the mice were intraperitoneally injected with EV-A71 at 1.7×10^7 PFU per mouse on day 0 and intraperitoneally injected with anti-HMGB1 at 5 μg per mouse on day 1 and day 3. On days 0, 2, 4, 5, 6, and 7, the mice were supplied to Von Frey test.

The recombinant proteins and neutralizing antibodies were listed in table S1.

Cell culture

Two human brain glioblastoma cell lines include T98G and U87MG, human neuroblastoma cell line SH-SY5Y, human colorectal (HT-29) cells, human RD cells, and Vero cells (African green monkey kidney cells) were purchased from the American Type Culture Collection. All cell lines were cultured in Dulbecco's modified Eagle's medium (DMEM) (HyClone, Logan, UT, USA) containing 10% fetal bovine serum (FBS; Gibco, Carlsbad, CA, USA) and 1% penicillin-streptomycin (P/S) solution (NCM Biotech, Suzhou, China) at 37°C with a 5% CO_2 humidified atmosphere.

Mouse primary astrocytes preparation and culture

Mouse primary astrocytes were prepared as described previously (*56*). First, the brain of mice was obtained, the cerebral cortices were isolated, and the meninges were removed. Second, the tissue was segmented, digested with tryptase (1004GR100, BioFroxx, Germany) plus deoxyribonuclease I (D8071, Solarbio, Beijing, China), and filtered using 70-μm cell strainer (352350, CORNING, NY, USA). Third, the cells were cultured in DMEM/F12 (Gibco, Carlsbad, CA, USA) medium supplemented with 10% FBS and 1% P/S to reach confluence. Last, astrocytes were obtained through shanking the flasks to remove most microglia. Harvested astrocytes were verified by immunofluorescence staining using antibody against astrocyte marker glial fibrillary acidic protein (GFAP) and microglia marker ionized calcium binding adaptor molecule 1 (IBA1).

Virus

The BrCr strain of EV-A71 was a gift from B. Wu at the Jiangsu Province Centers of Disease Control. Virus was propagated in Vero cells, and the viral titers were calculated as the 50% tissue culture infectious dose ($TCID_{50}$) using the Reed-Munch method as previously described (*25*). The multiplicity of infection (MOI) was specified in each figure legend.

RNA extraction and qPCR assays

Total RNA in cells or tissue samples was harvested using TRIzol reagent (Life Technologies, Carlsbad, USA), and then reverse-transcribed into cDNA using the PrimeScript RT Reagent Kit (TaKaRa, Kyoto, Japan). Quantitative polymerase chain reaction (qPCR) was performed using SYBR green qPCR Master mix (Vazyme biotech, Nanjing, China) on Applied Biosystems 7500 system as previously described (*57*). Relative mRNA levels were calculated using $2^{-\Delta\Delta Ct}$ method and normalized to β actin mRNA levels. All the used primers were listed in table S2. Absolute qPCR was performed using SYBR green qPCR Master mix on Applied Biosystems 7500 system as previously described (*56*). Briefly, the linearized plasmid encoding generic EV71 5′ untranslated region (5′UTR) (pT7-EV71-5′UTR), which was generated by our group (*58*), was serial diluted to generate the standard curve and then detected by EV-A71–5′UTR (listed in table S2). Samples were set up in a 96-well PCR amplification plate along with plasmid standards and no-template controls, and the virus copy numbers in samples were determined by the standard curve in the same plate.

Enzyme-linked immunosorbent assay

The concentration of LCN2 in mouse tissue homogenization, serum, and cell culture supernatants was measured by Mouse LCN2 enzyme-linked immunosorbent assay (ELISA) kit (S203682, D&B Biological Science and Technology, Shanghai, China; RK03063, Abclonal, Wuhan, China), HMGB1 concentration in mouse serum was measured by a mouse HMGB1 ELISA kit (S203674, D&B Biological Science and Technology, Shanghai, China), and LCN2 concentration in human cell culture supernatants was measured by a human LCN2 ELISA kit (RK10078, Abclonal, Wuhan, China) according to the manufacturers' instructions.

Tissue processing and Immunofluorescence

Harvested tissues were fixed overnight with 4% paraformaldehyde (PFA), dehydrated, embedded in paraffin, and sectioned. Then, the slides were deparaffinized, rehydrated, antigen restored, and followed by incubation with 2% bovine serum albumin (BSA) for 1 hour. Next, the sections were stained by the TSAPLus Fluorescent Triple Staining Kit (G1236, Servicebio, Wuhan, China) according to manufacturer's protocol. Then, the nuclei were stained with 4′,6-diamidino-2-phenylindole (DAPI). Whole brain slices were scanned by 3DHISTECH (Pannoramic MIDI), and the sections were also imaged by Olympus Fluoview FV3000, and the intensity of fluorescence was measured by ImageJ software. The used primary antibodies were listed in table S1.

Cell Immunofluorescence

Harvested cells were fixed with 4% PFA, permeabilized with 0.5% Triton X-100, and followed by blocking with 2% BSA. Next, the cells were incubated with specific antibodies at 4°C overnight and then incubated with Alexa Fluro 594–labeled donkey anti-rabbit IgG (R37119, Thermo Fisher Scientific, USA) about 1 hour. The nuclei were stained with DAPI. The cells were observed and imaged by Olympus Fluoview FV3000 and analyzed with ImageJ software. The used primary antibodies were listed in table S1.

HMGB1 neutralization model

As for the neutralization of HMGB1 in EV-A71–infected mouse serum, the serum harvested in EV-A71–infected AG6 mice at 0 and 4 dpi was UV-treated for 30 min, and each 75 μl of serum was added to 1 ml of medium and then added to 2- to 3-day-old AG6 mice–derived primary astrocytes, which were incubated with anti-HMGB1 (10 μg/ml) and control IgM for 24 hours.

As for the neutralization of HMGB1 in EV-A71–infected HT-29 supernatants, HT-29 cells were infected with EV-A71 (MOI = 1) and incubated with anti-HMGB1 (10 μg/ml) or control IgM for 36 hours, and then the cell supernatants were collected for 30-min UV treatment and then added 10 μl to Vero cell for 24-hour testing. In 24-hour testing, the images of Vero cells showed the cytopathic effects (CPEs) of EV-A71 in Vero cells. After testing, the rest of the UV-treated supernatants were added to U87MG cells for 24 hours.

LCN2 neutralization model

As for the neutralization of LCN2 in EV-A71–infected U87MG supernatants, U87MG cells were infected with EV-A71 (MOI = 0.5) for 24 hours in the presence of anti-LCN2 (4.5 μg/ml) or control IgG. Then, the cell supernatants were collected for 30-min UV treatment and added to Vero cells for 24-hour testing. In 24-hour testing, the images of Vero cells showed the CPEs of EV-A71 in Vero cells. After testing, the rest of the supernatants were added to RD cells for 24 hours.

Plasmids transfection

Plasmid pLV2-*Lcn2*-EGFP-Puro (P43850) and control plasmid pLV2-CMV-EGFP-Puro (P45317) were purchased from MIAOLING BIOLOGY (Wuhan, China). RD cells were transfected with the above plasmids using Lipofectamine 8000 reagent (C0533, Beyotime, Shanghai, China) according to the manufacturer's instructions.

Biochemical activity examination

The harvested mouse tissues or harvested cells were washed twice by phosphate-buffered saline (PBS) and then homogenized in matching proportion of lysate. The glucose, lactate, pyruvate, and ATP in homogenized tissues or cells were determined using the Glucose

Detection Kit (S0201S, Beyotime, Shanghai, China), the Lactate Detection Kit (A019-2-1, Nanjing Jiancheng, Nanjing, China), the Pyruvate Detection Kit (A081-1-1, Nanjing Jiancheng, Nanjing, China), and the ATP Detection Kit (S0026, Beyotime, Shanghai, China) according to the manufacturer's protocol, separately.

The HK (BC0740), PDH (BC0380), and LDH (BC0685) Activity Assay Kits were purchased from Solarbio (Beijing, China) and were used to examine the biological activity of the corresponding enzyme.

ECAR/OCR assay

The ATP production rate and extracellular acidification of RD cells was measured as their oxygen consumption rate (OCR) or ECAR on an oxygen-controlled XF96 extracellular flux analyzer (Seahorse Bioscience) following the manufacturer's protocols. Briefly, RD cells were seeded on XF96 microplates (Agilent, CA, USA) and were cultured in a humidified incubator at 37°C supplied with 5% CO_2. After the experimental treatment, the cells were applied for next detection. The ATP production rate of RD cells was measured using the XF Real-Time ATP Rate Assay Kit (103592-100, Seahorse Bioscience) according to the protocol. Briefly, the cells were maintained with assay medium plus 1 mM pyruvate, 2 mM glutamine, and 5 mM glucose (Seahorse Bioscience) in a none-CO_2 incubator for 45 min before the assay, and the oligomycin (final concentration of 1.5 μM) and rotenone/antimycin (final concentration of 0.5 μM) were sequentially injected into the medium. The extracellular acidification under basal conditions was measured using the XF Glycolysis Stress Test Kit (103020-100, Seahorse Bioscience) according the protocol. Briefly, the cells were maintained with assay medium plus 2 mM glutamine and 5 mM glucose (Seahorse Bioscience) in a none-CO_2 incubator for 45 min and then tested by the analyzer. All the data were normalized to cellular protein concentration after the assays.

Glucose uptake assay

Treated cells in 12-well plates were washed once with ice-cold PBS and then trypsinized and centrifuged for 3 min at 1000 rpm, and then the cells were incubated with 100 μM 2-NBDG working solution (using sterile PBS configuration) at 37°C for 1 hour. Cells not treated with 2-NBDG served as a negative control. The cells were then washed twice with ice-cold PBS and resuspended in 1 ml of PBS for flow cytometry analysis (NovoCyte FACS system, Agilent), and the 2-NBDG uptake was measured using fluorescein isothiocyanate (FITC) channels. For each measurement, data from 10,000 single-cell events were collected. The data were normalized to the mean fluorescence intensity of FITC and analyzed using FlowJo software (version 10.8).

Dataset re-analysis

Four datasets in NCBI-GEO DataSets were re-analyzed for DEGs, and the criteria for selecting up-regulated DEGs after viral infection was $\log_2FC \geq 2$. GSE44331 evaluated the DEGs between VSV-infected and mock-infected *WT* mice from brain at 5 dpi, GSE154002 evaluated the DEGs between JEV-infected and mock-infected *WT* mice from brain until mice developed clinical symptoms of viral encephalitis, GSE123550 evaluated the DEGs between EV-A71–infected and mock-infected gerbils from brain at 4 dpi, and GSE136221 evaluated the DEGs between WNV-infected and mock-infected *WT* mice from brain at 5 dpi. Bioinformatic analysis including Wayne's map, heatmap, and GO enrichment barplot was performed using the OmicStudio tools at www.omicstudio.cn/tool.

Statistical analysis

Except for the animal studies (one time), each experiment was repeated at least three times. All data were analyzed using GraphPad Prism version 8.0 (GraphPad Software, San Diego, CA, USA). Error bars on all graphs and tables represent the SEM. Statistical significance was tested using Student's *t* tests and one-way analysis of variance (ANOVA), followed by a Student–Newman–Keuls *q* test. $^*P < 0.05$ represents the statistical significance (ns, not significant; $^{**}P < 0.01$; $^{***}P < 0.001$; and $^{****}P < 0.0001$).

Supplementary Materials

This PDF file includes:

Figs. S1 to S9
Tables S1 and S2

REFERENCES AND NOTES

1. Z. Ślebioda, B. Dorocka-Bobkowska, Hand, foot and mouth disease as an emerging public health problem: Case report of familial child-to-adult transmission. *Dent. Med. Probl.* **55**, 99–104 (2018).
2. S. Poenaru, S. J. Abdallah, V. Corrales-Medina, J. Cowan, COVID-19 and post-infectious myalgic encephalomyelitis/chronic fatigue syndrome: A narrative review. *Ther. Adv. Infect. Dis.* **8**, 20499361211009385 (2021).
3. K. Bartholomeeusen, M. Daniel, D. A. LaBeaud, P. Gasque, R. W. Peeling, K. E. Stephenson, L. F. P. Ng, K. K. Ariën, Chikungunya fever. *Nat. Rev. Dis. Primers* **9**, 17 (2023).
4. T. M. Sharp, M. Fischer, J. L. Muñoz-Jordán, G. Paz-Bailey, J. E. Staples, C. J. Gregory, S. H. Waterman, Dengue and Zika virus diagnostic testing for patients with a clinically compatible illness and risk for infection with both viruses. *MMWR Recomm. Rep.* **68**, 1–10 (2019).
5. F. Wang, Y. Wu, J. Jiao, J. Wang, Z. Ge, Risk factors and clinical characteristics of severe fever with thrombocytopenia syndrome. *Int. J. Gen. Med.* **13**, 1661–1667 (2020).
6. C. Huang, Y. Wang, X. Li, L. Ren, J. Zhao, Y. Hu, L. Zhang, G. Fan, J. Xu, X. Gu, Z. Cheng, T. Yu, J. Xia, Y. Wei, W. Wu, X. Xie, W. Yin, H. Li, M. Liu, Y. Xiao, H. Gao, L. Guo, J. Xie, G. Wang, R. Jiang, Z. Gao, Q. Jin, J. Wang, B. Cao, Clinical features of patients infected with 2019 novel coronavirus in Wuhan, China. *Lancet* **395**, 497–506 (2020).
7. G. Narayanappa, B. N. Nandeesh, Infective myositis. *Brain Pathol.* **31**, e12950 (2021).
8. T. Aschman, J. Schneider, S. Greuel, J. Meinhardt, S. Streit, H. H. Goebel, I. Büttnerova, S. Elezkurtaj, F. Scheibe, J. Radke, C. Meisel, C. Drosten, H. Radbruch, F. L. Heppner, V. M. Corman, W. Stenzel, Association between SARS-CoV-2 infection and immune-mediated myopathy in patients who have died. *JAMA Neurol.* **78**, 948–960 (2021).
9. J. Raber, E. M. Rhea, W. A. Banks, The effects of viruses on insulin sensitivity and blood-brain barrier function. *Int. J. Mol. Sci.* **24**, 2377 (2023).
10. S. Yang, M. Tian, Y. Dai, R. Wang, S. Yamada, S. Feng, Y. Wang, D. Chhangani, T. Ou, W. Li, X. Guo, J. McAdow, D. E. Rincon-Limas, X. Yin, W. Tai, G. Cheng, A. Johnson, Infection and chronic disease activate a systemic brain-muscle signaling axis. *Sci. Immunol.* **9**, eadm7908 (2024).
11. B. K. Jung, Y. Park, B. Yoon, J. S. Bae, S. W. Han, J. E. Heo, D. E. Kim, K. Y. Ryu, Reduced secretion of LCN2 (lipocalin 2) from reactive astrocytes through autophagic and proteasomal regulation alleviates inflammatory stress and neuronal damage. *Autophagy* **19**, 2296–2317 (2023).
12. E. V. Mike, H. M. Makinde, M. Gulinello, K. Vanarsa, L. Herlitz, G. Gadhvi, D. R. Winter, C. Mohan, J. G. Hanly, C. C. Mok, C. M. Cuda, C. Putterman, Lipocalin-2 is a pathogenic determinant and biomarker of neuropsychiatric lupus. *J. Autoimmun.* **96**, 59–73 (2019).
13. K. W. Poh, J. F. Yeo, C. S. Stohler, W. Y. Ong, Comprehensive gene expression profiling in the prefrontal cortex links immune activation and neutrophil infiltration to antinociception. *J. Neurosci.* **32**, 35–45 (2012).
14. S. Jeon, M. K. Jha, J. Ock, J. Seo, M. Jin, H. Cho, W. H. Lee, K. Suk, Role of lipocalin-2-chemokine axis in the development of neuropathic pain following peripheral nerve injury. *J. Biol. Chem.* **288**, 24116–24127 (2013).
15. M. K. Jha, S. Jeon, M. Jin, J. Ock, J. H. Kim, W. H. Lee, K. Suk, The pivotal role played by lipocalin-2 in chronic inflammatory pain. *Exp. Neurol.* **254**, 41–53 (2014).
16. M. K. Jha, S. Jeon, M. Jin, W. H. Lee, K. Suk, Acute phase protein Lipocalin-2 is associated with formalin-induced nociception and pathological pain. *Immune Netw.* **13**, 289–294 (2013).
17. S. L. Kim, S. T. Lee, I. S. Min, Y. R. Park, J. H. Lee, D. G. Kim, S. W. Kim, Lipocalin 2 negatively regulates cell proliferation and epithelial to mesenchymal transition through changing metabolic gene expression in colorectal cancer. *Cancer Sci.* **108**, 2176–2186 (2017).

18. A. Bhusal, M. H. Rahman, W. H. Lee, I. K. Lee, K. Suk, Satellite glia as a critical component of diabetic neuropathy: Role of lipocalin-2 and pyruvate dehydrogenase kinase-2 axis in the dorsal root ganglion. *Glia* **69**, 971–996 (2021).
19. Y. Wen, X. Chen, H. Feng, X. Wang, X. Kang, P. Zhao, C. Zhao, Y. Wei, Kdm6a deficiency in microglia/macrophages epigenetically silences Lcn2 expression and reduces photoreceptor dysfunction in diabetic retinopathy. *Metabolism* **136**, 155293 (2022).
20. P. Koo, J. M. Sethi, Metabolic Myopathies and the Respiratory System. *Clin. Chest Med.* **39**, 401–410 (2018).
21. J. Yagi, H. N. Wenk, L. A. Naves, E. W. McCleskey, Sustained currents through ASIC3 ion channels at the modest pH changes that occur during myocardial ischemia. *Circ. Res.* **99**, 501–509 (2006).
22. D. C. Immke, E. W. McCleskey, Lactate enhances the acid-sensing Na+ channel on ischemia-sensing neurons. *Nat. Neurosci.* **4**, 869–870 (2001).
23. R. Haas, J. Smith, V. Rocher-Ros, S. Nadkarni, T. Montero-Melendez, F. D'Acquisto, E. J. Bland, M. Bombardieri, C. Pitzalis, M. Perretti, F. M. Marelli-Berg, C. Mauro, Lactate regulates metabolic and pro-inflammatory circuits in control of t cell migration and effector functions. *PLOS Biol.* **13**, e1002202 (2015).
24. M. K. Jha, G. J. Song, M. G. Lee, N. H. Jeoung, Y. Go, R. A. Harris, D. H. Park, H. Kook, I. K. Lee, K. Suk, Metabolic connection of inflammatory pain: Pivotal role of a pyruvate dehydrogenase kinase-pyruvate dehydrogenase-lactic acid axis. *J. Neurosci.* **35**, 14353–14369 (2015).
25. Q. You, J. Wu, Y. Liu, F. Zhang, N. Jiang, X. Tian, Y. Cai, E. Yang, R. Lyu, N. Zheng, D. Chen, Z. Wu, HMGB1 release induced by EV71 infection exacerbates blood-brain barrier Disruption via VE-cadherin phosphorylation. *Virus Res.* **338**, 199240 (2023).
26. Y. Zhang, Z. Zhu, W. Yang, J. Ren, X. Tan, Y. Wang, N. Mao, S. Xu, S. Zhu, A. Cui, Y. Zhang, D. Yan, Q. Li, X. Dong, J. Zhang, Y. Zhao, J. Wan, Z. Feng, J. Sun, S. Wang, D. Li, W. Xu, An emerging recombinant human enterovirus 71 responsible for the 2008 outbreak of hand foot and mouth disease in Fuyang city of China. *Virol. J.* **7**, 94 (2010).
27. D. Chen, X. Tian, X. Zou, S. Xu, H. Wang, N. Zheng, Z. Wu, Harmine, a small molecule derived from natural sources, inhibits enterovirus 71 replication by targeting NF-κB pathway. *Int. Immunopharmacol.* **60**, 111–120 (2018).
28. J. Liu, Y. Liu, K. Nie, S. Du, J. Qiu, X. Pang, P. Wang, G. Cheng, Flavivirus NS1 protein in infected host sera enhances viral acquisition by mosquitoes. *Nat. Microbiol.* **1**, 16087 (2016).
29. A. López-Sánchez, B. Guijarro Guijarro, G. Hernández Vallejo, Human repercussions of foot and mouth disease and other similar viral diseases. *Med. Oral* **8**, 26–32 (2003).
30. S. Chakraborty, E. Sen, A. Basu, Pyruvate dehydrogenase kinase 1 promotes neuronal apoptosis upon Japanese encephalitis virus infection. *IBRO Neurosci. Rep.* **13**, 410–419 (2022).
31. N. P. Lindsey, J. E. Staples, J. A. Lehman, M. Fischer, Centers for Disease Control and Prevention (CDC), Surveillance for human West Nile virus disease - United States, 1999-2008. *MMWR Surveill. Summ.* **59**, 1–17 (2010).
32. Z. Huang, H. Li, S. Liu, J. Jia, Y. Zheng, B. Cao, Identification of neutrophil-related factor LCN2 for predicting severity of patients with influenza a virus and SARS-CoV-2 infection. *Front. Microbiol.* **13**, 854172 (2022).
33. J. M. Lawrence, K. Schardien, B. Wigdahl, M. R. Nonnemacher, Roles of neuropathology-associated reactive astrocytes: A systematic review. *Acta Neuropathol. Commun.* **11**, 42 (2023).
34. Z. Luo, R. Su, W. Wang, Y. Liang, X. Zeng, M. A. Shereen, N. Bashir, Q. Zhang, L. Zhao, K. Wu, Y. Liu, J. Wu, EV71 infection induces neurodegeneration via activating TLR7 signaling and IL-6 production. *PLOS Pathog.* **15**, e1008142 (2019).
35. S. A. Jaberi, A. Cohen, C. D'Souza, Y. M. Abdulrazzaq, S. Ojha, S. Bastaki, E. A. Adeghate, Lipocalin-2: Structure, function, distribution and role in metabolic disorders. *Biomed. Pharmacother.* **142**, 112002 (2021).
36. K. A. Pollak, J. D. Swenson, T. A. Vanhaitsma, R. W. Hughen, D. Jo, A. T. White, K. C. Light, P. Schweinhardt, M. Amann, A. R. Light, Exogenously applied muscle metabolites synergistically evoke sensations of muscle fatigue and pain in human subjects. *Exp. Physiol.* **99**, 368–380 (2014).
37. V. P. Tan, S. Miyamoto, HK2/hexokinase-II integrates glycolysis and autophagy to confer cellular protection. *Autophagy* **11**, 963–964 (2015).
38. J. Chen, M. Zhang, Y. Liu, S. Zhao, Y. Wang, M. Wang, W. Niu, F. Jin, Z. Li, Histone lactylation driven by mROS-mediated glycolytic shift promotes hypoxic pulmonary hypertension. *J. Mol. Cell Biol.* **14**, mjac073 (2023).
39. Z. M. Kohler, G. Trencsenyi, L. Juhasz, A. Zvara, J. P. Szabo, L. Dux, L. G. Puskas, L. Rovo, A. Keller-Pinter, Tilorone increases glucose uptake in vivo and in skeletal muscle cells by enhancing Akt2/AS160 signaling and glucose transporter levels. *J. Cell. Physiol.* **238**, 1080–1094 (2023).
40. G. B. Clements, F. McGarry, C. Nairn, D. N. Galbraith, Detection of enterovirus-specific RNA in serum: The relationship to chronic fatigue. *J. Med. Virol.* **45**, 156–161 (1995).
41. S. Qin, Y. Li, L. Wang, X. Zhao, X. Ma, G. F. Gao, Assessment of vaccinations and breakthrough infections after adjustment of the dynamic zero-COVID-19 strategy in China: An online survey. *Emerg. Microbes Infect.* **12**, 2258232 (2023).
42. J. Sawatzky, J. Soo, A. L. Conroy, R. Bhargava, S. Namasopo, R. O. Opoka, M. T. Hawkes, Biomarkers of Systemic Inflammation in Ugandan Infants and Children Hospitalized With Respiratory Syncytial Virus Infection. *Pediatr. Infect. Dis. J.* **38**, 854–859 (2019).
43. X. Ding, S. Li, L. Zhu, Potential effects of HMGB1 on viral replication and virus infection-induced inflammatory responses: A promising therapeutic target for virus infection-induced inflammatory diseases. *Cytokine Growth Factor Rev.* **62**, 54–61 (2021).
44. J. Zhang, Z. Wang, H. Zhang, S. Li, J. Li, H. Liu, Q. Cheng, The role of lipocalin 2 in brain injury and recovery after ischemic and hemorrhagic stroke. *Front. Mol. Neurosci.* **15**, 930526 (2022).
45. X. Xu, H. N. Piao, F. Aosai, X. Y. Zeng, J. H. Cheng, Y. X. Cui, J. Li, J. Ma, H. R. Piao, X. Jin, L. X. Piao, Arctigenin protects against depression by inhibiting microglial activation and neuroinflammation via HMGB1/TLR4/NF-κB and TNF-α/TNFR1/NF-κB pathways. *Br. J. Pharmacol.* **177**, 5224–5245 (2020).
46. J. Pouysségur, I. Marchiq, S. K. Parks, J. Durivault, M. Ždralević, M. Vucetic, 'Warburg effect' controls tumor growth, bacterial, viral infections and immunity - Genetic deconstruction and therapeutic perspectives. *Semin. Cancer Biol.* **86**, 334–346 (2022).
47. J. D. Rabinowitz, S. Enerbäck, Lactate: The ugly duckling of energy metabolism. *Nat. Metab.* **2**, 566–571 (2020).
48. R. Muraleedharan, M. V. Gawali, D. Tiwari, A. Sukumaran, N. Oatman, J. Anderson, D. Nardini, M. A. N. Bhuiyan, I. Tkáč, A. L. Ward, M. Kundu, R. Waclaw, L. M. Chow, C. Gross, R. Rao, S. Schirmeier, B. Dasgupta, AMPK-regulated astrocytic lactate shuttle plays a non-cell-autonomous role in neuronal survival. *Cell Rep.* **32**, 108092 (2020).
49. F. Bi, C. Huang, J. Tong, G. Qiu, B. Huang, Q. Wu, F. Li, Z. Xu, R. Bowser, X. G. Xia, H. Zhou, Reactive astrocytes secrete lcn2 to promote neuron death. *Proc. Natl. Acad. Sci. U.S.A.* **110**, 4069–4074 (2013).
50. H. Rindt, Z. Feng, C. Mazzasette, J. J. Glascock, D. Valdivia, N. Pyles, T. O. Crawford, K. J. Swoboda, T. N. Patitucci, A. D. Ebert, C. J. Sumner, C. P. Ko, C. L. Lorson, Astrocytes influence the severity of spinal muscular atrophy. *Hum. Mol. Genet.* **24**, 4094–4102 (2015).
51. W. I. Zhi, R. E. Baser, D. Talukder, Y. Z. Mei, S. E. Harte, T. Bao, Mechanistic and thermal characterization of acupuncture for chemotherapy-induced peripheral neuropathy as measured by quantitative sensory testing. *Breast Cancer Res. Treat.* **197**, 535–545 (2023).
52. S. R. Chaplan, F. W. Bach, J. W. Pogrel, J. M. Chung, T. L. Yaksh, Quantitative assessment of tactile allodynia in the rat paw. *J. Neurosci. Methods* **53**, 55–63 (1994).
53. C. Mills, D. Leblond, S. Joshi, C. Zhu, G. Hsieh, P. Jacobson, M. Meyer, M. Decker, Estimating efficacy and drug ED50's using von Frey thresholds: Impact of weber's law and log transformation. *J. Pain* **13**, 519–523 (2012).
54. H. Li, P. Liu, S. Deng, L. Zhu, X. Cao, X. Bao, S. Xia, Y. Xu, B. Zhang, Pharmacological upregulation of microglial lipid droplet alleviates neuroinflammation and acute ischemic brain injury. *Inflammation* **46**, 1832–1848 (2023).
55. S. B. Dunnett, S. P. Brooks, Motor assessment in huntington's disease mice. *Methods Mol. Biol.* **1780**, 121–141 (2018).
56. H. Wang, M. Yuan, E. Yang, D. Chen, A. Su, Z. Wu, Enterovirus 71 infection induced Aquaporin-4 depolarization by increasing matrix metalloproteinase-9 activity. *Neurosci. Lett.* **759**, 136049 (2021).
57. J. Wu, Q. You, R. Lyu, Y. Qian, H. Tao, F. Zhang, Y. Cai, N. Jiang, N. Zheng, D. Chen, Z. Wu, Folate metabolism negatively regulates OAS-mediated antiviral innate immunity via ADAR3/endogenous dsRNA pathway. *Metabolism* **143**, 155526 (2023).
58. H. Wang, L. Chang, X. Wang, A. Su, C. Feng, Y. Fu, D. Chen, N. Zheng, Z. Wu, MOV10 interacts with Enterovirus 71 genomic 5'UTR and modulates viral replication. *Biochem. Biophys. Res. Commun.* **479**, 571–577 (2016).

Acknowledgments: We thank Y. Xu at Department of Neurology of Nanjing Drum Tower Hospital and C. Lai at the Department of Neurology of Affiliated Jinling Hospital for the help in this work. **Funding:** This work was supported by the National Natural Science Foundation of China (U22A20335 and 31970149 to Z.W. and 81900823 to D.C.), the Major Research and Development Project (2018ZX10301406 to Z.W.), and the Reserve Talents Project of Young Academic and Technical Leaders in Yunnan Province (202405 AC350028 to M.H.).
Author contributions: Conceptualization: Z.W., Q.Y., J.W., D.C., S.D., and M.H. Methodology: Q.Y., J.W., C.W., Y.C., N.Z., R.L., Y.Q., and M.H. Investigation: Q.Y., J.W., and C.W. Data curation: Z.W., Q.Y., J.W., and S.D. Validation: Q.Y., J.W., and S.D. Formal analysis: Q.Y., J.W., and S.D. Software: Q.Y., J.W., and S.D. Visualization: Q.Y., J.W., D.C., and S.D. Resources: Z.W., M.H., and Y.X. Funding acquisition: Z.W., M.H., and D.C. Supervision: Z.W. Project administration: Z.W. Writing—original draft: Q.Y., J.W., D.C., and S.D. Writing—review and editing: Z.W., and M.H.
Competing interests: The authors declare that they have no competing interests. **Data and materials availability:** All data needed to evaluate the conclusions in the paper are present in the paper and/or the Supplementary Materials.

Submitted 19 October 2024
Accepted 11 April 2025
Published 16 May 2025
10.1126/sciadv.adt9837